

Minkowski Functionals of the 21 cm Signal as a Probe of Primordial Features

Kanan Virkar,^{a,b,1} Suvedha Suresh Naik,^{c,a,2} Pravabati Chingangbam^{a,b,3}

^aIndian Institute of Astrophysics, Koramangala II Block, Bangalore 560 034, India.

^bDepartment of Physics, Pondicherry University, R.V. Nagar, Kalapet, 605 014, Puducherry, India

^cKorea Institute for Advanced Study (KIAS), 85 Hoegiro, Dongdaemun-gu, Seoul, Republic of Korea-02455

E-mail: kanan.virkar@iiap.res.in, suvedha@kias.re.kr, prava@iiap.res.in

Abstract. The redshifted 21 cm signal from the cosmic dawn and Epoch of Reionization (EoR) encodes important information about both astrophysical processes and primordial physics, such as inflation. In this work, we use morphological statistics to explore the sensitivity of the 21 cm signal to inflationary features and EoR dynamics simultaneously. Focusing on primordial features from particle production during inflation we generate semi-numerical simulations of the 21 cm signal across redshifts $5 \lesssim z \lesssim 35$, incorporating these features. Using Minkowski Functionals (MFs), we analyze the morphology of 21 cm fields: density, neutral hydrogen fraction, spin temperature, and brightness temperature. We demonstrate that MFs are highly sensitive to both the amplitude and scale of primordial features, capturing rich morphological information. In particular, we show that MFs can robustly identify inflationary features and distinguish them from the standard model. We further explore various EoR scenarios, and demonstrate that combining MFs across redshifts can disentangle the signatures of primordial features from EoR effects. This approach opens new avenues for probing inflation with upcoming 21 cm surveys.

Contents

1	Introduction	1
2	Physics of inflationary particle production and reionization	3
2.1	Particle production during inflation	3
2.2	Physics and simulation of the 21 cm signal	4
3	Minkowski Functionals and their behaviour for the fiducial model	7
3.1	Morphology of EoR fields for the fiducial model	8
4	Results - effects of particle production during inflation	10
4.1	Background: Imprints of bump models on the 21 cm signal	11
4.1.1	MFs of the density field	12
4.1.2	MFs of the spin temperature field	14
4.1.3	MFs of the neutral hydrogen field	15
4.1.4	MFs of the brightness temperature field	16
5	Distinguishability of primordial features from astrophysical parameters	18
5.1	Effects of astrophysical parameters	18
5.2	Quantifying morphological differences	20
6	Summary and Discussion	24
A	Effect of primordial bump-like features on the halo mass function	26

1 Introduction

The first billion years after the Big Bang is an important period in cosmology during which the first stars, galaxies and the large scale structure formed through hierarchical structure formation. These early luminous sources ionized the neutral hydrogen surrounding them, and by around $z \sim 6$ almost all of the neutral hydrogen in the universe was ionized. This period, known as the epoch of reionization (EoR), spans from the cosmic dawn (when the first stars formed) to the end of reionization. Despite its cosmological significance, this epoch remains relatively unexplored observationally. However, recent observational efforts by modern telescopes like JWST shed light on early galaxies up to redshift $z \sim 14$ [1]. The high-redshift frontier has also been extended through observations of Lyman- α forest from high-redshift quasars that reveal properties of intervening neutral hydrogen clouds [2]. One of the most promising probes of this epoch is the 21 cm signal from neutral hydrogen. This signal is produced by the hyperfine transition in the ground state of neutral hydrogen in the radio band ($\lambda \sim 21$ cm or $\nu \sim 1420$ MHz). Since neutral hydrogen is the most abundant baryonic component in the early universe, the 21 cm signal provides direct information about the thermal and ionisation state of the intergalactic medium (IGM), the properties of early luminous sources, and the underlying cosmology (see, e.g., [3, 4] for reviews).

The distribution of neutral hydrogen during the cosmic dawn and EoR is sensitive to the seed initial density fluctuations set by inflation. A large class of inflationary models predict

deviations from a nearly scale-invariant form of the primordial power spectrum, commonly referred to as ‘primordial features’ (see [5] for a review). The 21 cm signal then offers a unique window into primordial density fluctuations, besides its sensitivity to astrophysical processes, providing complementary probes of inflationary signatures alongside the CMB and large-scale structure observations. Additionally, the 21 cm signal has been proposed as a probe of dark matter properties (see, e.g., [6, 7] and refs. therein), primordial non-Gaussianity [8–12], and other beyond-standard-model physics.

In this work, we focus on bump-like features in the primordial power spectrum arising from particle production during inflation [13–19]. Such features can leave distinct imprints on the observables such as CMB anisotropy [20] and 21 cm signal, as they modify the reionisation history and the distribution of structures depending on the scale at which the feature occurs [21, 22]. However, in [22] it was found that at specific scales – namely the turnover scale – bump models are indistinguishable from the fiducial model in their globally averaged 21 cm profile. It is therefore of importance to investigate whether other statistical measures can detect these features. As these features are theoretically well motivated, identifying their observational signatures is essential for probing the physics of inflation and the origin of primordial density fluctuations.

Several ongoing and upcoming radio interferometers aim to detect the 21 cm signal from the EoR, including LOFAR [23], MWA [24], HERA [25], and the SKA [26]. The SKA, in particular, will carry out the deepest observations of neutral hydrogen, tracing the evolution of cosmic structure over the redshift range $6 < z < 30$. These observations will yield three-dimensional maps of the 21 cm brightness temperature, enabling detailed studies of the EoR morphology. Extracting cosmological and astrophysical information from these maps requires appropriate statistical tools. The 21 cm signal from the EoR is expected to be highly non-Gaussian due to the patchy nature of reionisation; consequently, the globally averaged signal and power spectrum do not capture the full information content. Higher-order statistics, such as the bispectrum [9, 27–32] and morphological descriptors, are therefore essential for fully characterising the signal.

Minkowski functionals (MFs) [33–36] are a powerful set of morphological descriptors that characterise the geometry and topology of random fields. In three dimensions, the four MFs quantify the volume fraction, surface area, mean curvature, and Euler characteristic of excursion sets at different thresholds. MFs have been extensively applied to study reionisation models using the 21 cm signal [37–42], extending beyond the genus [43]. Minkowski tensors [44–50] and Betti numbers [48–54] further provide additional information. These studies have demonstrated that MFs are sensitive to the ionisation topology and can distinguish between different reionisation scenarios. However, the imprints of primordial features on the morphology of the 21 cm signal have not yet been explored. Since bump-like features in the primordial power spectrum enhance density fluctuations at specific scales, they are expected to modify the clustering of matter and consequently the morphology of the 21 cm signal. Thus, this approach will open up new avenues for probing inflation with upcoming 21 cm surveys.

In this work, we employ MFs to investigate the signatures of primordial bump-like features on the 21 cm signal from the EoR. Our objectives are threefold: (i) to characterise how bump models modify the morphology of the density, spin temperature, neutral hydrogen, and brightness temperature fields; (ii) to determine whether MFs can distinguish bump models – particularly at the “turnover scale” where the global signal is insensitive – from the fiducial model; and (iii) to examine whether primordial signatures can be distinguished from

variations in astrophysical parameters governing the EoR.

We modify the initial conditions of the semi-numerical simulation code `21cmFAST v3` [55, 56] to incorporate bump-like features and compute MFs on the resulting three-dimensional fields. We find that MFs are highly sensitive to both the amplitude and location of primordial features, and can distinguish bump models from the fiducial case across a wide range of redshifts. Crucially, MFs can identify bump models at the turnover scale, where the global 21 cm signal of reionisation history is indistinguishable from the fiducial model. Furthermore, by comparing the morphological signatures of primordial features with those of EoR parameter variations, we identify redshift ranges where the two can be distinguished, demonstrating the potential of MFs for constraining inflationary physics with future SKA observations.

The paper is organized as follows. Section 2 presents overviews of the physics of inflationary particle production, and the epoch of reionisation, along with the semi-numerical simulations used in this work. Section 3 presents the definitions of Minkowski functionals, along with a summary of their redshift evolution for the key fields of the EoR for the case of a fiducial model. Section 4 presents our results on the morphological signatures of inflationary particle production for fixed EoR physics. Section 5 explores potential degeneracies between inflationary particle production and EoR physics. We conclude with a summary of our main results and discussion in section 6.

2 Physics of inflationary particle production and reionization

In this section, we provide an overview of the inflationary particle production mechanism central to this work. We then review the physics governing cosmic dawn and the EoR, and describe our simulation framework for modeling the high-redshift 21 cm signal.

2.1 Particle production during inflation

We focus on a class of inflationary models involving bursts of particle production during inflation, which predict bump-like features in the primordial power spectrum [13–16]. Such particle production mechanisms are well motivated in inflation models based on higher-dimensional gauge theories [17–19]. The resulting power spectrum can be written approximately as [16, 20]

$$\mathcal{P}_{\mathcal{R}}(k) = A_s \left(\frac{k}{k_0} \right)^{n_s-1} + A_I \sum_i \left(\frac{f_1(x_i)}{f_1^{\max}} \right) + A_{II} \sum_i \left(\frac{f_2(x_i)}{f_2^{\max}} \right), \quad (2.1)$$

where A_s is the amplitude of the scalar perturbations, n_s is the scalar spectral index, $k_0 = 0.05 \text{ Mpc}^{-1}$, is the pivot scale, and A_I and A_{II} are the amplitudes of the dominant and subdominant contributions from particle production, respectively. The scale dependence of these contributions is given by the dimensionless functions

$$f_1(x_i) \equiv \frac{[\sin(x_i) - \text{Si}(x_i)]^2}{x_i^3}, \quad f_2(x_i) \equiv \frac{-2x_i \cos(2x_i) + (1 - x_i^2) \sin(2x_i)}{x_i^3}, \quad (2.2)$$

where $x_i \equiv k/k_i$, and $\text{Si}(x) \equiv \int_0^x \frac{\sin t}{t} dt$ is the sine integral. The functions $f_1(x)$ and $f_2(x)$ attain their maximum values at $f_1^{\max} \simeq 0.11$ and $f_2^{\max} \simeq 0.85$, respectively. The parameter $k_i (\text{Mpc}^{-1})$ specifies the location of the i^{th} feature in the primordial power spectrum. The peak of the i^{th} dominant contribution occurs at

$$k_{\text{peak},i} \simeq 3.35 \times k_i, \quad (2.3)$$

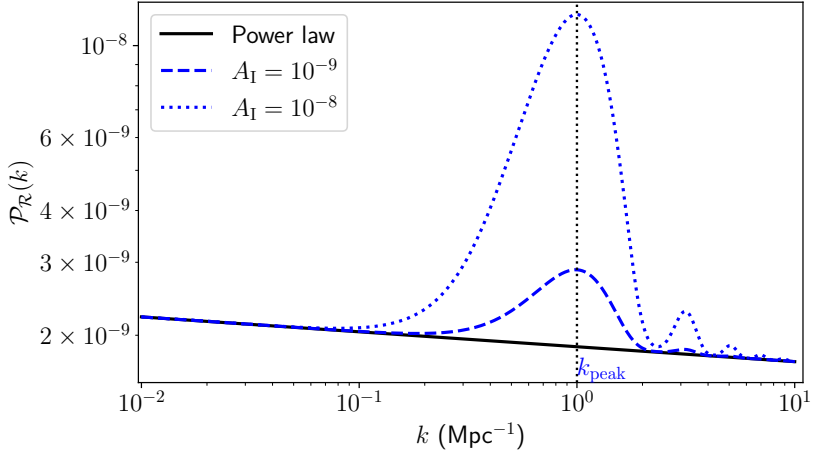


Figure 1: The primordial power spectrum with a bump-like primary feature at $k_{\text{peak}} = 1 \text{ Mpc}^{-1}$ arising from particle production during inflation.

while the subdominant contribution peaks at $x_i \simeq 1.25$. In this work, we consider a single burst of particle production during inflation, resulting in bump-like features parameterised by the amplitude A_{I} ¹ and the peak location k_{peak} (Mpc^{-1}).

The signatures of bump-like features have been investigated using CMB data from the *Planck* satellite [20], which placed upper limits on their amplitudes over comoving wavenumbers $2 \times 10^{-4} \lesssim k (\text{Mpc}^{-1}) \lesssim 0.15$. The impact of such features on the 21 cm signal has been examined through both the 21 cm power spectrum [21] and the globally averaged signal [22], demonstrating the potential of upcoming 21 cm observations to constrain these models. While ongoing experiments primarily target measurements of the global signal and power spectrum, mapping the 21 cm brightness temperature field can provide complementary information. The 21 cm signal from cosmic dawn and the EoR is expected to be inherently non-Gaussian, and inflationary models predicting primordial features can introduce additional non-Gaussianity [16]. It is therefore essential to employ multiple statistical measures to fully characterise the signal.

2.2 Physics and simulation of the 21 cm signal

The 21 cm signal from neutral hydrogen at a given redshift z is observed along the line of sight against a background radio source, which at high redshifts is predominantly the CMB. The differential brightness temperature associated with the 21 cm signal is defined as the difference between the brightness temperature of the hydrogen cloud and the CMB temperature, and is given by [57]:

$$\delta T_b(\vec{x}, z) \approx 27 x_{\text{HI}} (1 + \delta_b) \left(\frac{H}{dv_r/dr + H} \right) \left(1 - \frac{T_\gamma}{T_S} \right) \left(\frac{1+z}{10} \frac{0.15}{\Omega_M h^2} \right)^{1/2} \left(\frac{\Omega_b h^2}{0.023} \right) \text{mK}, \quad (2.4)$$

where x_{HI} is the neutral hydrogen fraction, δ_b is the baryon overdensity, dv_r/dr is the co-moving velocity gradient along the line of sight, T_γ is the CMB temperature, and T_S is the

¹The subdominant amplitude is not an independent parameter and is related to A_{I} by $A_{\text{II}} \simeq (2.9 \times 10^{-6}) A_{\text{I}}^{5/7} [\ln A_{\text{I}}^{4/7} + 24]$.

spin temperature, which characterizes the excitation of the 21 cm hyperfine transition. In subsequent parts of the paper we will refer to δ_b simply as ‘density field’ as is commonly done.

From eq. (2.4), we see that the detectability of the 21 cm signal depends critically on the spin temperature; the signal is observable only when it deviates from the CMB temperature. The spin temperature encodes information about the underlying astrophysical processes and is determined by three competing mechanisms: (i) absorption and emission of 21 cm photons from the radio background, primarily the CMB; (ii) collisions with other hydrogen atoms and with free electrons; and (iii) resonant scattering of Ly α photons, which induces spin flips via an intermediate excited state (the Wouthuysen–Field effect). Since the rates of these processes are fast compared to the Hubble time, the spin temperature can be well approximated by the equilibrium condition (see, e.g., [57–59] for a detailed explanation):

$$T_S^{-1} = \frac{T_\gamma^{-1} + x_\alpha T_\alpha^{-1} + x_c T_K^{-1}}{1 + x_\alpha + x_c}, \quad (2.5)$$

where T_α is the color temperature of the Ly α radiation field, T_K is the gas kinetic temperature ($T_\alpha \approx T_K$ in most astrophysical conditions), x_c is the collisional coupling coefficient, and x_α is the Ly α coupling coefficient (Wouthuysen–Field coupling).

Simulations of reionization

To model the cosmological fields entering eq. (2.4), we employ `21cmFAST v3`² [55, 56], a semi-numerical simulation tool widely used for generating cosmological 21 cm signals. The code produces three-dimensional realisations of the evolved density field δ_b , neutral hydrogen fraction x_{HI} , comoving peculiar velocity gradient dv_r/dr , and spin temperature T_S , which are then combined to compute the 21 cm brightness temperature δT_b via eq. (2.4).

The brightness temperature is sensitive to various astrophysical processes, which are parameterised in `21cmFAST` as follows:

- T_{vir} (K): the minimum virial temperature of haloes hosting star-forming galaxies, equivalently characterised by the cut-off mass M_{min} below which star formation is negligible;
- ζ : the ionising efficiency of high-redshift galaxies, which depends on the escape fraction of ionising photons f_{esc} , its power-law scaling with halo mass α_{esc} , the star formation efficiency f_* , its power-law scaling with halo mass α_* , the number of ionising photons per baryon N_γ , the typical number of recombinations n_{rec} , and the star formation timescale t_* (expressed as a fraction of the Hubble time);
- $L_{X<2\text{ keV}}/\text{SFR}$: the soft-band X-ray luminosity (below 2 keV) per unit star formation rate and the minimum energy of X-ray photons that can escape the host galaxy E_0 .

We simulate the 21 cm signal along with the underlying cosmological fields (δ_b , x_{HI} , and T_S) over the redshift range $z = 5 - 35$. The resulting maps are smoothed with a Gaussian kernel to a resolution of 6 Mpc, and we calculate the morphological statistics of these smoothed fields. As our baseline, we consider a fiducial model without primordial features, adopting a power-law primordial power spectrum and fixing the astrophysical parameters to $\zeta = 30$, $T_{\text{vir}} = 4.69 \times 10^4$ K, and $\log(L_X/\text{erg s}^{-1}) = 40.5$, as summarised in table 1. To investigate signatures of the inflationary models with bump-like features in the 21 cm

²<https://github.com/21cmfast/21cmFAST>

Parameters	Model	Values/Range
Simulation		Box length = 300 Mpc
		Resolution = 3 Mpc
		Redshift range: $z = 5 - 35$
		Smoothing scale = 6 Mpc
Background cosmology		$\Omega_\Lambda = 0.72, \Omega_M = 0.28, \Omega_b = 0.046, H_0 = 70 \text{ km s}^{-1} \text{ Mpc}^{-1}$
Primordial power spectrum	Fiducial	$\ln(10^{10} A_s) = 3.044, n_s = 0.965, \sigma_8 = 0.811$
	Bump models	$A_I \in [10^{-9}, 10^{-8}], k_{\text{peak}} \in [0.4, 0.5, 0.6] \text{ Mpc}^{-1}$
Astrophysical parameters	Fiducial	$\zeta = 30, T_{\text{vir}} = 4.69 \times 10^4 \text{ K}, \log(L_X/\text{erg s}^{-1}) = 40.5$
	EoR models	$\zeta \in [20, 45], T_{\text{vir}} \in [4.5, 5.0] \times 10^4 \text{ K}, \log(L_X/\text{erg s}^{-1}) \in [38.5, 41]$

Table 1: Simulation configuration and model parameters used in this work.

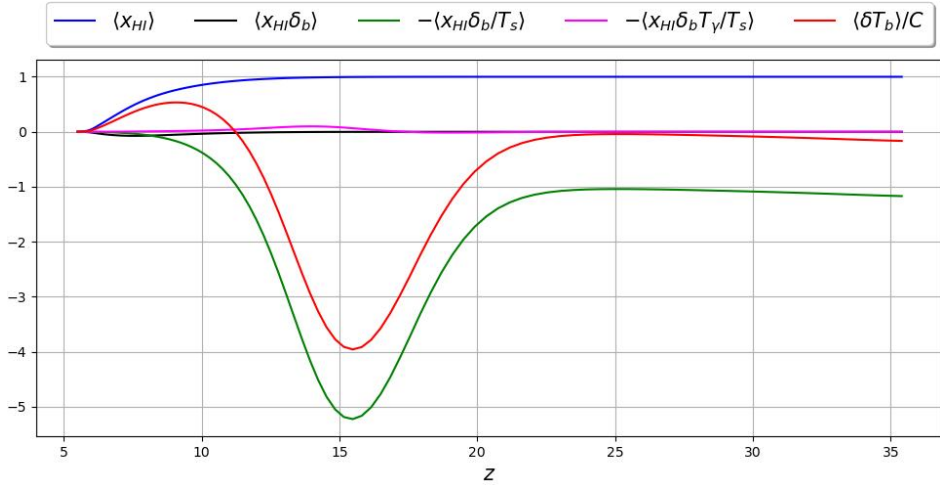


Figure 2: Redshift dependence of the mean values of different terms that contribute to the mean brightness temperature (see eq. (2.6)). The spatially constant quantity C is defined by eq. (2.7).

signal, we incorporate the corresponding primordial power spectrum (figure 1) into the initial conditions and generate the cosmological fields. We refer to such models hereafter as “bump models”.

The effects of bump models were recently studied in detail using the global 21 cm signal in ref. [22], which demonstrated the ability of global 21 cm profiles to discriminate between the effects of different values of amplitude A_I and location of the bump k_{peak} . However, for primordial features located near a “turnover scale”, $k_{\text{peak}} \simeq k^{\text{turn}}$, the global signal shows no effects of them regardless of redshift. We therefore examine bump models in this regime using Minkowski functionals, which can provide complementary constraining power. Specifically, we consider $k_{\text{peak}} \in \{0.4, 0.5, 0.6\} \text{ Mpc}^{-1}$, which includes the turnover scale $k^{\text{turn}} \simeq 0.5 \text{ Mpc}^{-1}$ for the EoR parameters listed in Table 1 [22]. For the amplitude, we consider $A_I \in \{10^{-9}, 10^{-8}\}$, consistent with the upper limit $A_I \lesssim 10^{-8}$ obtained from the global 21 cm signal using the optical depth to reionisation measured by *Planck* (see figure 11 of Ref. [22]).

To understand the redshift-dependent physical contributions to δT_b , we expand the right-

hand side of eq. (2.4) as a sum of constituent terms and take the spatial average. This gives

$$\frac{1}{C} \langle \delta T_b(\vec{x}, z) \rangle = \langle x_{\text{HI}} \rangle + \langle x_{\text{HI}} \delta_b \rangle - \left\langle \frac{x_{\text{HI}} \delta_b}{T_S} \right\rangle - \left\langle \frac{x_{\text{HI}} \delta_b T_\gamma}{T_S} \right\rangle, \quad (2.6)$$

where the spatially constant prefactor C is defined as

$$C = 27 \left(\frac{1+z}{10} \frac{0.15}{\Omega_M h^2} \right)^{1/2} \left(\frac{\Omega_b h^2}{0.023} \right). \quad (2.7)$$

The redshift evolution of each term on the right-hand side of eq. (2.6) is plotted in figure 2 for the fiducial primordial and EoR model. Since the velocity gradient $dv_r/dr \ll H$, we set the factor containing it to unity. From the figure, we see that different terms dominate at different epochs. At early times ($z > 20$), the contribution to δT_b arises primarily from δ_b and T_S , while $x_{\text{HI}} \approx 1$. At intermediate redshifts ($10 \lesssim z \lesssim 20$), the third term (green curve) dominates as both x_{HI} and T_S contribute significantly. At lower redshifts ($z < 10$), δT_b approximately traces x_{HI} . Although this classification into high, intermediate, and low redshift regimes is approximate and model-dependent, we adopt it in subsequent sections to organise our results.

3 Minkowski Functionals and their behaviour for the fiducial model

In this section, we review the formalism of Minkowski functionals for three-dimensional fields. We then describe the information that can be extracted by applying them to the 3D realisations of the fiducial model described in section 2.2. This serves as a foundation for understanding the effects of inflationary signatures, which we examine in subsequent sections.

Given a smooth mean zero random field $f(\mathbf{x})$ with standard deviation σ_0 , the excursion set at threshold ν is defined to be the set $Q(\nu) = \{\mathbf{x} \mid f(\mathbf{x}) \geq \nu \sigma_0\}$. $Q(\nu)$ contains all spatial regions where the field value exceeds a chosen threshold value. One can probe the morphology of the field across different levels by varying ν . To quantify the geometry and topology of the excursion sets, we use the commonly used morphological statistics Minkowski Functionals (MFs). In three dimensions they are defined by the following volume averaged quantities,

$$V_0 = \frac{1}{V} \int_Q dV, \quad V_1 = \frac{1}{6V} \int_{\partial Q} dA, \quad V_2 = \frac{1}{3\pi V} \int_{\partial Q} G_2 dA, \quad V_3 = \frac{1}{4\pi^2 V} \int_{\partial Q} G_3 dA, \quad (3.1)$$

where ∂Q denotes the boundary surface defined by the condition $f = \nu \sigma_0$ and V is the total volume occupied by the field. For V_2 and V_3 , the integrands are the mean curvature G_2 , and the Gaussian curvature G_3 of the surface ∂Q . The four MFs describe the volume fraction (V_0), surface area density (V_1), integrated mean density (V_2) and integrated Gaussian curvature density (V_3) of ∂Q .

For a mildly non-Gaussian field, $V_i(\nu)$ takes the following simple closed form expressions as perturbative expansion in powers of σ_0 , keeping upto first order [36, 60]:

$$V_i(\nu) = \frac{1}{(2\pi)^{\frac{i+1}{2}}} \frac{\omega_3}{\omega_{3-i} \omega_i} \left(\frac{\sigma_1}{\sqrt{3} \sigma_0} \right)^i e^{-\nu^2/2} \left[H_{i-1}(\nu) + \left(\frac{1}{6} S^{(0)} H_{i+2}(\nu) + \frac{i}{3} S^{(1)} H_i(\nu) + \frac{i(i-1)}{6} S^{(2)} H_{i-2}(\nu) \right) \sigma_0 + O(\sigma_0^2) \right], \quad (3.2)$$

where $i = 0, \dots, 3$, $\sigma_1 = \langle |\nabla f|^2 \rangle$, $H_n(\nu)$ are the probabilist Hermite polynomials, $H_{-1} = \sqrt{\frac{\pi}{2}} e^{\frac{\nu^2}{2}} \text{erfc}\left(\frac{\nu}{\sqrt{2}}\right)$, and $\omega_0 = 1$, $\omega_1 = 2$, $\omega_2 = \pi$ and $\omega_3 = \frac{4\pi}{3}$. The quantities $S^{(j)}$ are the generalized skewness parameters defined by:

$$S^{(0)} \equiv \frac{\langle f^3 \rangle}{\sigma_0^4}, \quad S^{(1)} \equiv -\frac{3}{4} \frac{\langle f^2 (\nabla^2 f) \rangle}{\sigma_0^2 \sigma_1^2}, \quad S^{(2)} \equiv -\frac{9}{4} \frac{\langle (\nabla f) \cdot (\nabla f) (\nabla^2 f) \rangle}{\sigma_1^4}. \quad (3.3)$$

For Gaussian fields, eq. (3.2) further simplifies because terms of order σ_0 and higher are zero.

Here the random field $f(\vec{x})$ can be one of the cosmological fields - density field ($\delta_b(\vec{x}, z)$), neutral hydrogen fraction ($x_{\text{HI}}(\vec{x}, z)$), spin temperature ($T_S(\vec{x}, z)$), brightness temperature fluctuation ($\delta T_b(\vec{x}, z)$). These fields have spatial fluctuations as well as redshift dependence. The variation of the amplitudes and shapes of the MFs with redshift encode how different physical effects affect the fields, and can be used to distinguish different primordial and EoR models. In general, the fields are non-Gaussian and the shapes of the MFs will depart from the Gaussian expectations. We will see in the next subsection that δ_b is mildly non-Gaussian at the redshifts and smoothing scales studied here, and their MFs can be described by eq. (3.2). In contrast, the other fields are strongly non-Gaussian, for which perturbative expansions of the MFs about the Gaussian expectations are not applicable.

3.1 Morphology of EoR fields for the fiducial model

We first examine the morphology of the EoR fields for the fiducial model, which adopts a power-law primordial power spectrum without the bump-like feature and the astrophysical parameters listed in table 1. With this parameter set, reionization reaches 50% at $z = 7.57$ and completes by $z \sim 6$. The simulated fields from 21cmFAST are smoothed with a Gaussian filter to a resolution of 6 Mpc, and we compute the MFs on the smoothed fields at different threshold values ν using the publicly available code PyMIN³ [39]. Since the EoR fields do not have zero mean, in general, we use threshold values of the normalised field $\tilde{f} = \frac{f - \langle f \rangle}{\sigma_0}$. The features in the MFs of the brightness temperature encode information about structure formation and reionization through their dependence on the density field δ_b , spin temperature T_S and neutral fraction x_{HI} .

Minkowski functionals for fields on three-dimensional space have previously been used to investigate different EoR models and to constrain the astrophysical parameter space [37–39, 61]. Here, we elaborate on the morphology of each physical field that contributes to δT_b , namely, δ_b , T_S and x_{HI} , to understand how different quantities affect the morphology of the brightness temperature. Figure 3(a) shows the lightcones for these fields. The Minkowski functionals for the 3D coeval cubes - V_0 , V_1 , V_2 , and V_3 - are plotted in the rows of figure 3(b) at selected redshifts corresponding to key evolutionary stages (early structure formation, IGM heating, and the progression of reionization). We discuss each of these in detail below.

Density field: The density field and its MFs for the fiducial model are shown in the first row of panel (a) and first column of panel (b) of figure 3. The distribution of density field is nearly Gaussian at high redshift ($z \sim 35$), as the initial density fluctuations after recombination are assumed to be described by a Gaussian random field. Accordingly, the MFs closely follow the analytical expressions for a mildly non-Gaussian field given in equations (3.2). Deviations from Gaussianity are expected to increase with time due to the nonlinear growth of structures driven by gravitational clustering at lower redshifts. Although the redshift dependence of the

³<https://github.com/dkn16/pyMIN>.

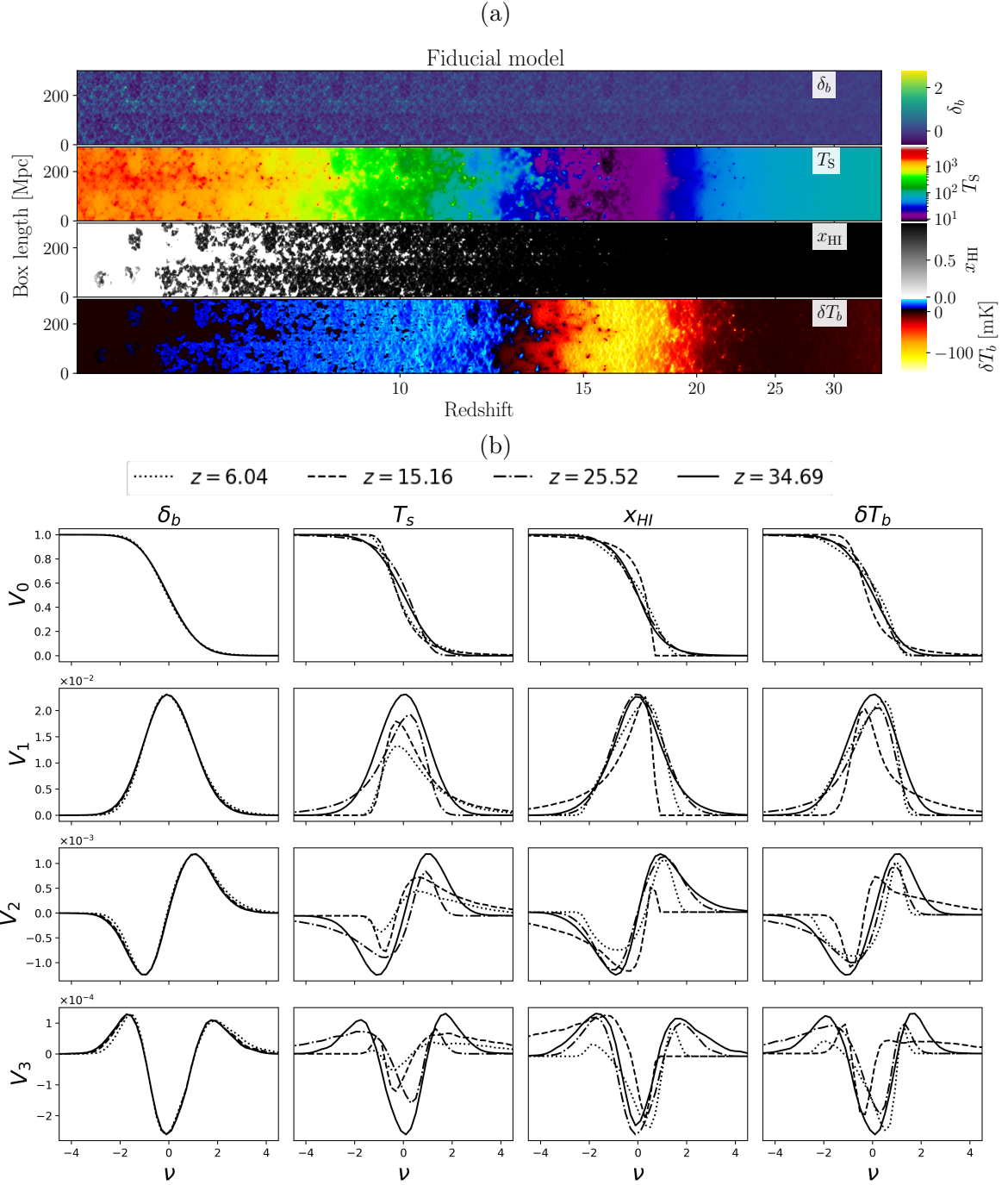


Figure 3: (a) Lightcones of δ_b , T_S , x_{HI} , and δT_b (rows) for the fiducial model; colours indicate the field values as shown by the respective colorbars. (b) Minkowski functionals V_0 , V_1 , V_2 , and V_3 (rows) as functions of threshold ν for the same fields as in panel (a) (columns), shown at selected redshifts indicated by different line styles in the legend.

MFs of the density field is mild, a slight increase in asymmetry of the MF curves from $z = 35$ (solid line) to $z = 6$ (dotted line) indicates the growing deviation from Gaussianity over time

(see discussion of the skewness parameters shown in figure 6 in section 4.1.1.) Consequently, the contribution of the density field to the redshift evolution of the brightness temperature morphology is expected to be minimal.

Spin temperature field: The MFs for T_S are shown in the second column of figure 3(b). At $z = 35$, the MFs of T_S closely follow those of δ_b . This is because, at such high redshifts, there are no Ly α sources, and spin temperature fluctuations arise solely from collisional coupling (x_c), which is proportional to the baryon density (cf. eq. (2.5)). At $z < 30$, Ly α coupling becomes significant and T_S becomes highly non-Gaussian, with deviations more pronounced than in δ_b across all four MFs. At $z \sim 25$, T_S couples to the gas kinetic temperature T_K , which is colder than the CMB ($T_K < T_\gamma$). Near overdense regions, fluctuations in both density and Ly α flux enhance this coupling, causing a sharp drop in T_S . This manifests as longer tails at negative thresholds in V_1 , V_2 , and V_3 . Conversely, at $z \lesssim 15$, heating from the first sources produces localised increases in T_S around overdense regions, leading to longer tails at positive thresholds. In addition to the change in the profile of the MF curves, their amplitudes also decrease with decreasing redshift, reflecting the reduced contrast in T_S fluctuations as heating progresses. Given this strong sensitivity to astrophysical processes, T_S is expected to be one of the dominant contributors to the morphology of the brightness temperature.

Neutral hydrogen field: As shown in the third column of figure 3(b), the MFs of the neutral hydrogen fraction x_{HI} follow those of δ_b at high redshifts, similar to T_S . This is expected since neutral hydrogen was the most abundant baryon species during this epoch, before ionising sources had formed. The field becomes non-Gaussian and negatively correlated with δ_b once the first sources begin ionising the surrounding medium, as seen in the curves for $z \lesssim 25$. At $z \sim 15$, the IGM is still nearly neutral (see the lightcone in panel (a) of figure 3), with only a few locally ionised regions as heating has just begun. This results in longer tails at negative thresholds with a sharp drop at higher ν . As V_2 characterises the connectivity of structures, it shows complex behaviour at lower redshifts due to percolation of ionised regions. By $z \sim 6$, the neutral fraction drops below 5%, with the IGM dominated by ionised regions; consequently, V_1 , V_2 , and V_3 decrease at negative thresholds. The peaks at positive thresholds correspond to the few remaining isolated neutral hydrogen islands. The strong evolution in x_{HI} morphology at lower redshifts directly drives the reionization signature in the brightness temperature field.

Brightness temperature field: As given in eq. (2.4), all the aforementioned fields contribute to the 21 cm signal. The MFs of δT_b are shown in the last column of figure 3(b). At $z \gtrsim 30$, fluctuations in δT_b follow those in δ_b . During the heating epoch ($15 \lesssim z \lesssim 25$), while most hydrogen remains neutral, δT_b is primarily driven by T_S . Once reionization commences ($z \lesssim 15$), x_{HI} fluctuations dominate; by $z \sim 6$ (dotted line), the MFs of δT_b closely follow those of x_{HI} . Thus, the MFs of δT_b trace the morphology of different contributing fields at different epochs. Having established this fiducial behaviour, we now examine how primordial features modify these MF signatures.

4 Results - effects of particle production during inflation

In this section, we present our results on the signatures of the bump model, characterised by the amplitude A_I and the primary peak location k_{peak} (see figure 1). The power spectrum in 21cmFAST is modified to include this feature according to eq. (2.1).

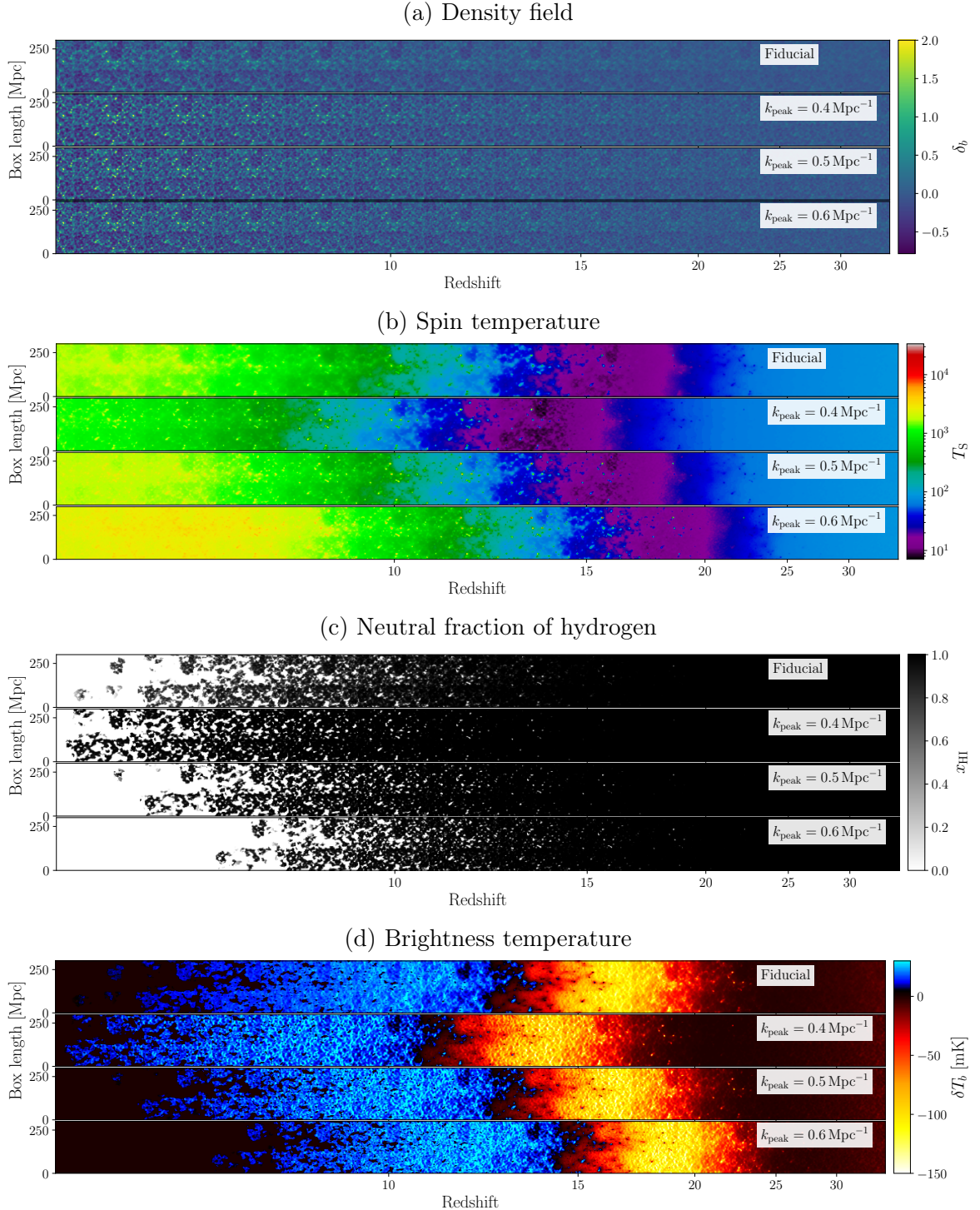


Figure 4: The simulated lightcones of all the fields for the fiducial and bump models.

4.1 Background: Imprints of bump models on the 21 cm signal

Before presenting our results on the morphology of fields for bump models, we briefly summarise their signatures on the 21 cm brightness temperature (see [21, 22] for details).

Eq. (2.4) informs that the 21 cm fluctuations of the brightness temperature are inherited from the fluctuations of δ_b , T_S , and x_{HI} . In 21cmFAST, the real-space density field is computed via an inverse Fourier transform of

$$\delta_b(\vec{k}) = \sqrt{\frac{VP(k)}{2}}(a_k + ib_k), \quad (4.1)$$

where V is the box volume, $P(k)$ is the matter power spectrum which includes the bump-like features, and a_k , b_k are Gaussian random variables with variance one [62]. Primordial features thus directly affect δT_b through δ_b : a feature at low (high) k_{peak} enhances overdensities on large (small) spatial scales.

Furthermore, it was demonstrated in [22] that primordial features significantly affect $x_{\text{HI}}(\vec{x}, z)$ and $T_S(\vec{x}, z)$. The value of k_{peak} plays a crucial role in determining the ionisation history: higher (lower) values of k_{peak} lead to faster (slower) structure formation and correspondingly earlier (later) completion of reionization. Increasing the amplitude of the feature enhances such effects. Remarkably, at a critical “turnover” scale $k_{\text{peak}} = k^{\text{turn}}$, bump-like features have negligible impact on the average reionization history and consequently on the globally averaged 21 cm signal. The lightcones illustrating the evolution of different fields for the fiducial and bump models are shown in figure 4; for the EoR parameters considered here, $k^{\text{turn}} = 0.5 \text{ Mpc}^{-1}$. The temporal evolution of the neutral hydrogen field in panel (c) clearly demonstrates how bump models modify structure formation and alter the reionization history relative to the fiducial model. This behaviour arises from the way primordial features modulate the collapsed fraction of haloes given by the halo mass function (HMF). Due to the power spectrum normalization at $8 \text{ h}^{-1} \text{Mpc}$, the enhancement of power at different scales introduced by the primordial features significantly alters the number density of halos. Features with low (high) k_{peak} amplify overdensities on large (small) scales, thereby suppressing (enhancing) the number density of low-mass haloes and resulting in slower (faster) structure formation (see appendix A for a summary of HMF modifications discussed in ref. [22]). The analysis in ref. [22] further revealed that k^{turn} depends on the value of T_{vir} since it sets the minimum halo mass for star formation, which in turn determines which scales dominate the ionisation budget.

With this understanding of how primordial features affect the 21 cm signal, our objectives are threefold: (i) to extract signatures of bump models directly from the morphology of the fields; (ii) to investigate whether bump models at $k_{\text{peak}} = k^{\text{turn}}$, which remain undetectable in the global 21 cm signal, can be distinguished from the fiducial model through MFs; and (iii) to examine distinctive signatures of primordial features compared to those of astrophysical processes during the EoR. We address objectives (i) and (ii) in this section and defer (iii) to the next section. To isolate the effects of primordial features on the MFs, we fix all EoR parameters to their fiducial values (table 1). We examine bump-like features with k_{peak} at and near the turnover scale, computing MFs for $k_{\text{peak}} [\text{Mpc}^{-1}] \in \{0.4, 0.5, 0.6\}$ and $A_I \in \{10^{-9}, 10^{-8}\}$.

4.1.1 MFs of the density field

The lightcones for the density fields of the bump models are shown alongside the fiducial model in panel (a) of figure 4. Although the effects of different k_{peak} values are barely discernible by visual inspection, quantitative analysis using MFs reveals clear differences in morphology. In figure 5, we present the MFs V_k at redshifts $z = 34.68$ and $z = 7.57$, spanning early and

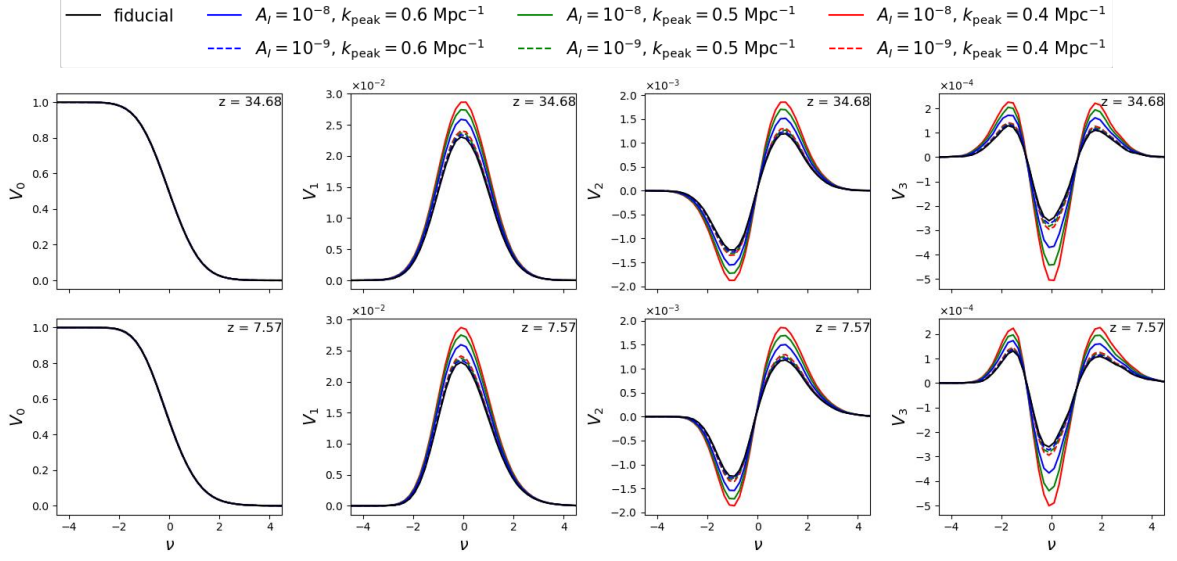


Figure 5: The Minkowski functionals for the density field $\delta_b(\vec{x})$ for models involving primordial bump-like features. The upper and lower panels show V_i at redshifts $z = 34.68$ and $z = 7.57$, respectively. The fiducial model is indicated by solid black line.

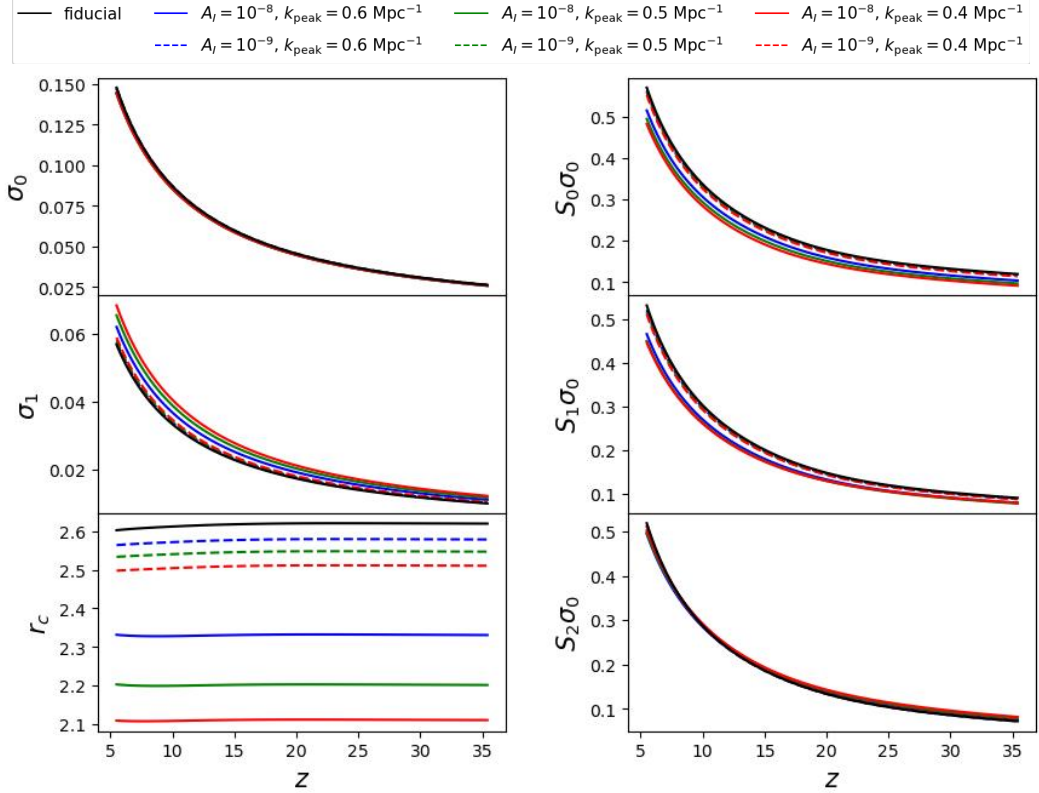


Figure 6: *Left:* redshift evolution of σ_0 , σ_1 and r_c for density field δ_b for the fiducial and bump models. *Right:* redshift evolution of $S^{(i)}\sigma_0$ for the same fields.

late epochs, respectively⁴.

As in the fiducial case, the profiles of MFs of the density field do not change significantly with redshift. However, bump models enhance the MF amplitudes relative to the fiducial model. This enhancement arises from additional morphological complexity introduced by primordial features, and is amplified by increasing A_1 . To understand this behaviour, we examine the quantities controlling the MF amplitudes. Since δ_b exhibits mild non-Gaussianity within our redshift range, the MF amplitudes are primarily determined by σ_0 (the field variance) and σ_1 (the variance of the field gradient). The ratio $r_c \equiv \sigma_0/\sigma_1$ defines a characteristic length scale of structures in the density field, with MF amplitudes scaling inversely as powers of r_c . The left column of figure 6 shows that both σ_0 and σ_1 grow with z at roughly the same rate, and hence r_c remains nearly independent of redshift, explaining the negligible temporal evolution in the MFs. The right column shows the three skewness parameters $S^{(i)}\sigma_0$ defined by eq. (3.3) (we show with the σ_0 factor since this gives the size of the non-Gaussian corrections, upto the Hermite polynomials and the constant prefactors). They grow with redshift as the density field becomes increasingly more non-Gaussian due to gravitational clustering. For the smoothing scale of 6 Mpc employed here we see that the density field is remains mildly non-Gaussian till $z \sim 6$, as indicated by the fact that $S^{(i)}\sigma_0$ remains below one.

The bump model with $k_{\text{peak}} = 0.4 \text{ Mpc}^{-1}$ exhibits the maximum deviation from the fiducial model due to its lowest r_c value. At our chosen smoothing scale, σ_0 values for all models coincide with the fiducial case, while σ_1 scales inversely with k_{peak} . Consequently, $r_c \propto k_{\text{peak}}$, leading to $V_k \propto 1/k_{\text{peak}}$. Thus, bump models with lower k_{peak} enhance large-scale overdensities, thereby increasing MF amplitudes. Conversely, for sufficiently high k_{peak} , the introduced small-scale overdensities are suppressed by the smoothing, resulting in negligible effects on the MFs. In summary, the MFs of δ_b are primarily sensitive to k_{peak} through its effect on the characteristic scale r_c of density structures.

4.1.2 MFs of the spin temperature field

The lightcones for T_S of the bump models are shown alongside the fiducial model in panel (b) of figure 4. One can observe strong variation with different k_{peak} values. The corresponding MFs are shown in figure 7. The behaviour varies significantly across redshift regimes:

- $z \sim 35$: The spin temperature field closely follows the density field due to the absence of heating and ionisation, as in the fiducial case. The MF amplitudes scale inversely with k_{peak} , as discussed for the density field.
- $z \sim 25$: In the fiducial model, the MFs exhibit extended tails toward negative thresholds. This is due to the drop in T_S around overdense regions which lead to an increase of the number of holes [49]. The bump models also follow this trend, with a special effect of k_{peak} . As k_{peak} increases, the MFs become increasingly asymmetric because faster structure formation results in more non-Gaussian characteristics in the T_S field. For $k_{\text{peak}} = 0.6 \text{ Mpc}^{-1}$, T_S drops within more localised regions, resulting in a sharper drop at positive thresholds, as seen in the T_S map in figure 4(b).
- $z \sim 16$: In the fiducial model, heating begins to affect the spin temperature, resulting in extended tails toward positive thresholds. This behaviour is also observed for $k_{\text{peak}} = 0.5$ and 0.6 Mpc^{-1} . However, for $k_{\text{peak}} = 0.4 \text{ Mpc}^{-1}$, slower structure formation delays the

⁴Since the MFs of the density field exhibit minimal redshift dependence, we present results at only two representative redshifts.

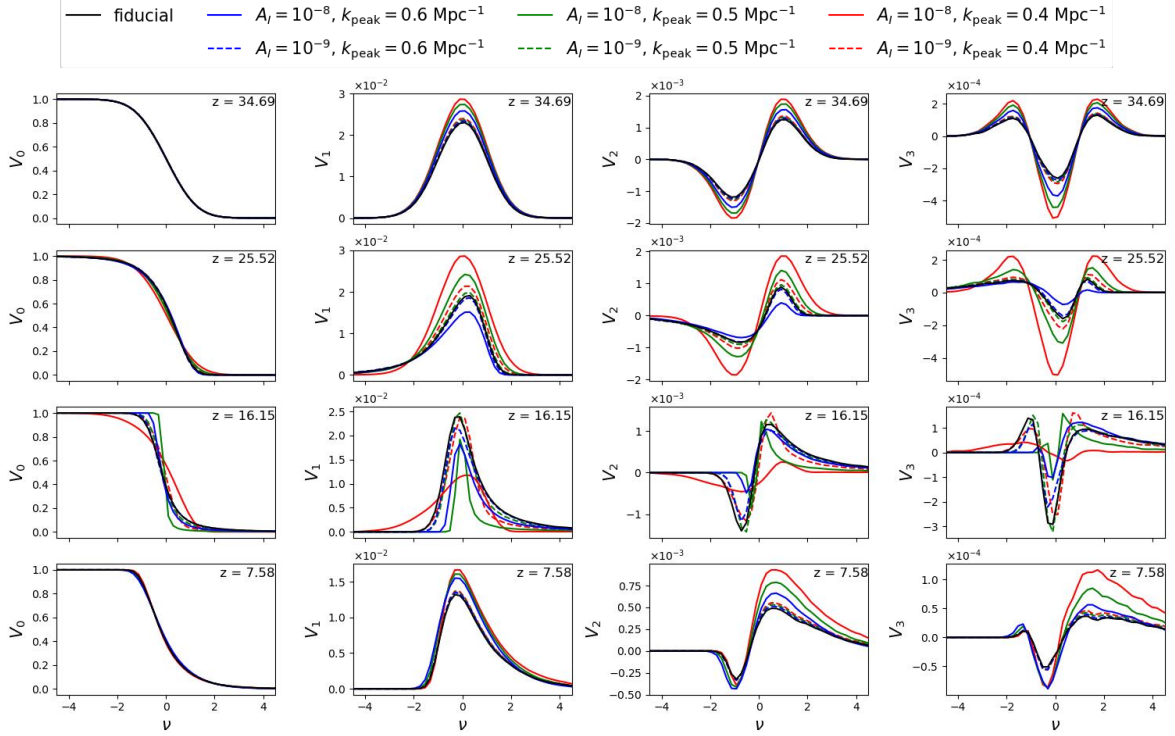


Figure 7: The Minkowski functionals for the spin temperature field $T_S(\vec{x})$ for models involving primordial bump-like features. The fiducial model is indicated by solid black line. The values of k_{peak} are denoted by different colors and the values of A_I are denoted by different linestyles.

onset of heating, and the T_S field has not yet risen sufficiently at this redshift. This results in distinctive MF behaviour compared to the other models.

- $z \sim 7.5$: At this stage, reionization reaches $\sim 50\%$ in the fiducial model. The lightcones show that T_S increases with higher k_{peak} , and consequently the MF curves exhibit extended tails toward positive thresholds.

In summary, the MFs of T_S are sensitive to k_{peak} through its effect on the timing of structure formation and heating.

4.1.3 MFs of the neutral hydrogen field

The lightcones for x_{HI} of all the models shown in panel (c) of figure 4 again exhibit strong variation with different k_{peak} values. The corresponding MFs are presented in figure 8. The behaviour varies across redshift regimes:

- $z \sim 35$: The neutral hydrogen field is nearly Gaussian and follows the density field, as in the fiducial case. The MF amplitudes scale inversely with k_{peak} , as discussed for the density field.
- $z \sim 25$: The fields remain close to Gaussian for all models except $k_{\text{peak}} = 0.6 \text{ Mpc}^{-1}$, which shows distinct departures from Gaussianity due to earlier formation of small-scale structures and low-mass haloes.

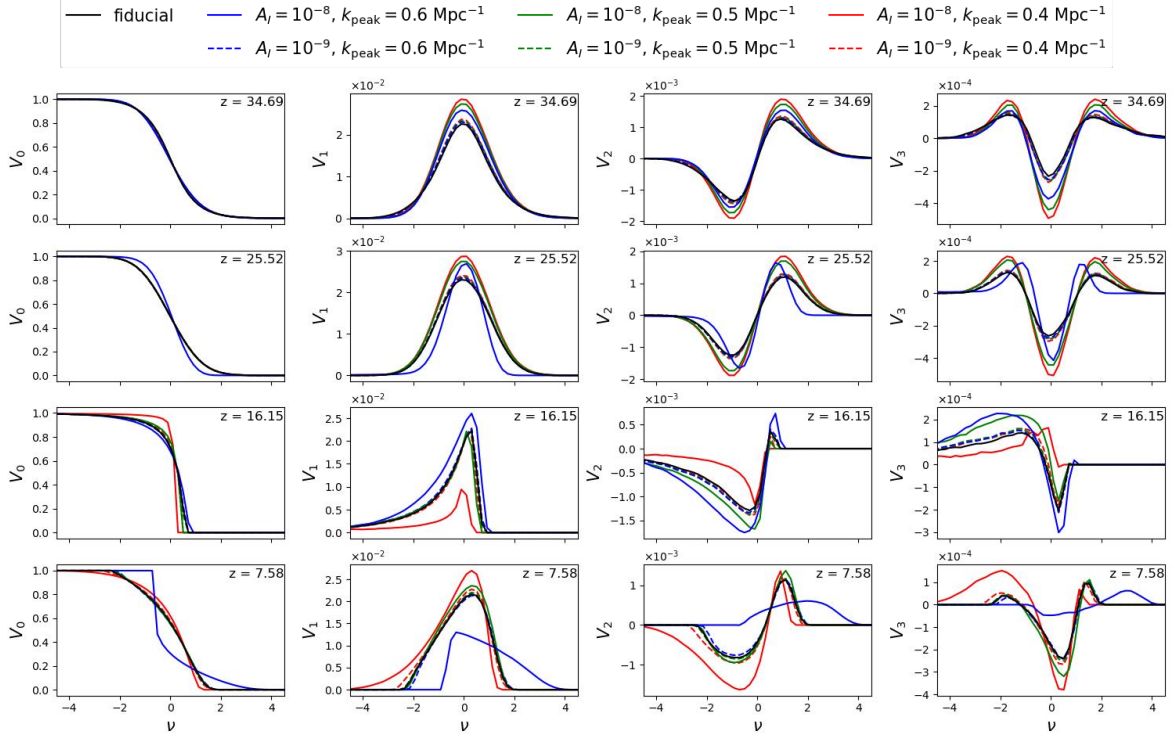


Figure 8: The Minkowski functionals for the neutral fraction of hydrogen $x_{\text{HI}}(\vec{x})$ for models involving primordial bump-like features. The fiducial model is indicated by solid black line. The values of k_{peak} are denoted by different colors and the values of A_I are denoted by different line styles.

- $z \sim 16$: Reionization proceeds faster for higher k_{peak} , producing more ionised regions. Consequently, $k_{\text{peak}} = 0.6 \text{ Mpc}^{-1}$ exhibits the largest MF amplitudes, while $k_{\text{peak}} = 0.4 \text{ Mpc}^{-1}$ displays the lowest.
- $z \sim 7.5$: At this redshift, which corresponds to 50% reionization in the fiducial model, the ionised fractions for $k_{\text{peak}} = 0.4, 0.5, \text{ and } 0.6 \text{ Mpc}^{-1}$ are 20%, 47%, and 86%, respectively. For $k_{\text{peak}} = 0.6 \text{ Mpc}^{-1}$, only scattered neutral islands remain, producing a peak at positive thresholds (most prominent in V_3). In contrast, for $k_{\text{peak}} = 0.4 \text{ Mpc}^{-1}$, the peak at positive thresholds arises from partially ionised regions as reionization progresses more slowly.

In summary, the MFs of x_{HI} are sensitive to k_{peak} through its effect on the timing and morphology of reionization.

4.1.4 MFs of the brightness temperature field

With insights from the preceding analysis of individual fields, we now examine the combined impact of bump models on the 21 cm signal. The lightcones depicting these effects are shown in figure 4(d). Visual inspection reveals significant morphological differences between bump models and the fiducial case, highlighting the potential for studying inflationary signatures in upcoming 21 cm brightness temperature maps.

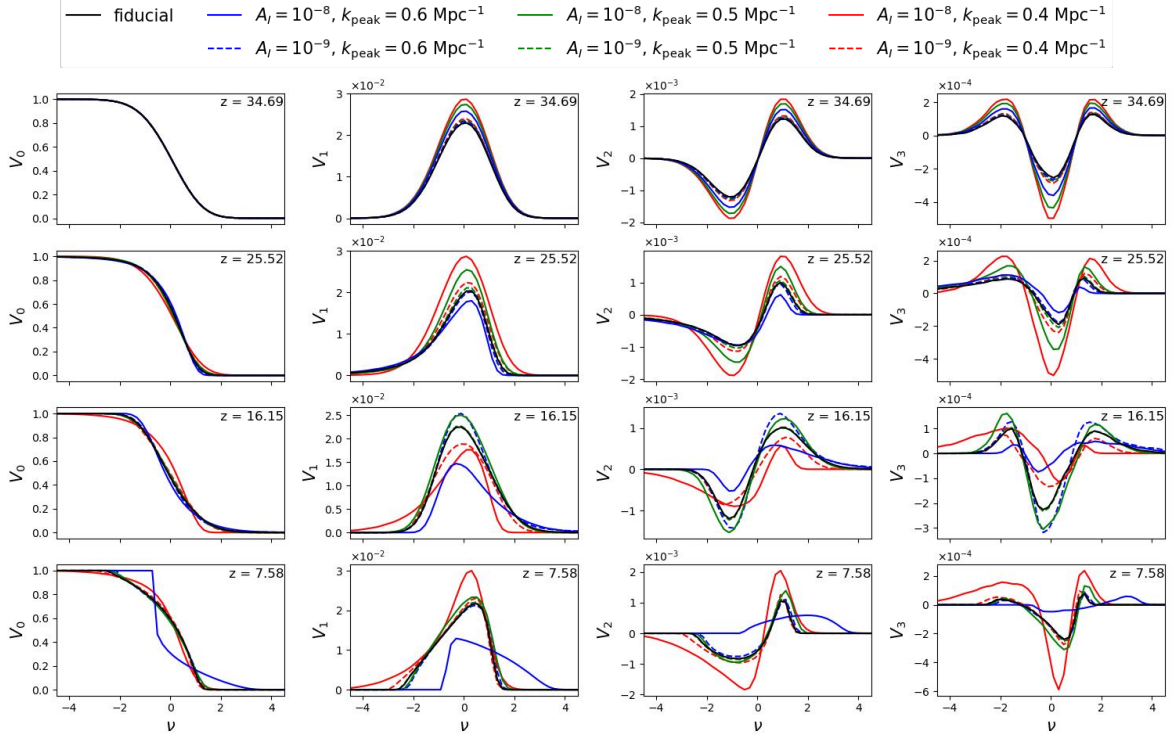


Figure 9: The Minkowski functionals for the brightness temperature of the 21 cm signal, $\delta T_b(\vec{x})$, for models involving primordial bump-like features. The fiducial model is indicated by solid black line. The values of k_{peak} are denoted by different colours and the values of A_1 are denoted by different line styles.

We present the MFs for bump models along with the fiducial model in figure 9. At different evolutionary stages, fluctuations in δT_b are dominated by different component fields as seen in figure 2 and also reflected in both the lightcones and MFs:

- $z \sim 35$: At this redshift, δT_b follows the density field δ_b (see figure 5). As discussed previously, fluctuations in δ_b are modulated by structures of different scales introduced through primordial features. For example, $k_{\text{peak}} = 0.4 \text{ Mpc}^{-1}$, which enhances large-scale structures, exhibits higher MF amplitudes compared to the other models.
- $z \sim 25$: As T_S begins coupling with T_K , fluctuations in δT_b follow those of T_S . Analogous to the analysis in section 4.1.2, all models except $k_{\text{peak}} = 0.4 \text{ Mpc}^{-1}$ have begun departing from the almost Gaussian nature of the field. The contributions from δ_b and x_{HI} fluctuations are subdominant at this stage.
- $z \sim 16$: Around this redshift, the brightness temperature fluctuations are influenced by all three component fields. The extended tail toward negative thresholds for $k_{\text{peak}} = 0.4 \text{ Mpc}^{-1}$ reflects the combined morphological influence of both T_S and x_{HI} . In the brightness temperature field, most regions exhibit absorption of the 21 cm signal, resulting in lower MF amplitudes at positive thresholds. For $k_{\text{peak}} = 0.6 \text{ Mpc}^{-1}$, the extended tail toward positive thresholds arises from localised emission regions due to relatively faster heating and reionization processes.

- $z \sim 7.5$: During the later stages of reionization, x_{HI} provides the dominant contribution to δT_b , as the 21 cm signal persists only at the neutral hydrogen islands that remain after ionised bubbles have merged to remove most neutral hydrogen from the universe. This effect is evident from both the lightcones and the MFs shown in the bottom rows of figures 8 and 9.

To summarise, the MFs of all fields – δ_b , T_S , x_{HI} , and δT_b – exhibit distinct signatures of bump-like primordial features. Lower k_{peak} enhances large-scale structures and increases MF amplitudes, while higher k_{peak} accelerates structure formation and reionization. The amplitude A_I primarily scales the magnitude of deviations from the fiducial model. However, the higher value $A_I = 10^{-8}$ does introduce additional changes of shape of the MFs. This can be attributed to the effect of the increased width of the primary bump, as well as the secondary bumps that become increasingly more prominent, as A_I increases (see figure 1). Crucially, MFs can distinguish bump models at the turnover scale $k^{\text{turn}} = 0.5 \text{ Mpc}^{-1}$ from the fiducial model, a regime where the models are indistinguishable from the reionization history and globally averaged 21 cm regime [22]. Importantly, this distinction arises because bump models modify the halo mass function across different mass scales (see figure 14 in Appendix A), altering the distribution of collapsing structures even when averaged quantities such as $\langle x_{\text{HI}} \rangle$ and $\langle \delta T_b \rangle$ remain unchanged. Thus, MFs capture morphological signatures inaccessible to global statistics, demonstrating their power for constraining primordial features. In the next section, we examine whether these inflationary signatures can be distinguished from variations in astrophysical parameters.

5 Distinguishability of primordial features from astrophysical parameters

Our analysis of bump models using MFs has demonstrated their sensitivity to both the amplitude A_I and the location k_{peak} of primordial features. However, a key question arises for observational applications: can primordial parameters be constrained simultaneously with the astrophysical parameters governing the high-redshift universe? Specifically, do primordial features and astrophysical variations produce degenerate MF signatures? We address this question by comparing the morphological signatures of EoR parameter variations with those of bump models, identifying redshift regimes where the two can be distinguished.

5.1 Effects of astrophysical parameters

In 21cmFAST, the astrophysical processes during the dark ages and EoR are modelled by several parameters, with key parameters discussed in section 2.2. We focus on three EoR parameters that significantly influence the ionisation history and consequently the evolution of the 21 cm signal: the ionising efficiency ζ , the virial temperature threshold T_{vir} , and the soft-band X-ray luminosity per unit SFR, L_X . The lightcones of the brightness temperature for variations in each of these parameters, in the range shown in table 1, are presented in figure 10. We highlight the major effects below:

- ζ : As shown in panel (a), ζ affects the 21 cm brightness temperature at $z \lesssim 15$. Increasing ζ enhances ionising photon production, accelerating reionization and leading to earlier completion. Although bump models with higher k_{peak} can also advance reionization, unlike ζ , the effects of k_{peak} are prominent at $z > 15$ as well.
- T_{vir} : Since T_{vir} sets the minimum halo mass for star formation, variations in T_{vir} affect a broader redshift range than ζ . Increasing T_{vir} from $\mathcal{O}(10^4) \text{ K}$ to $\mathcal{O}(10^5) \text{ K}$ shifts

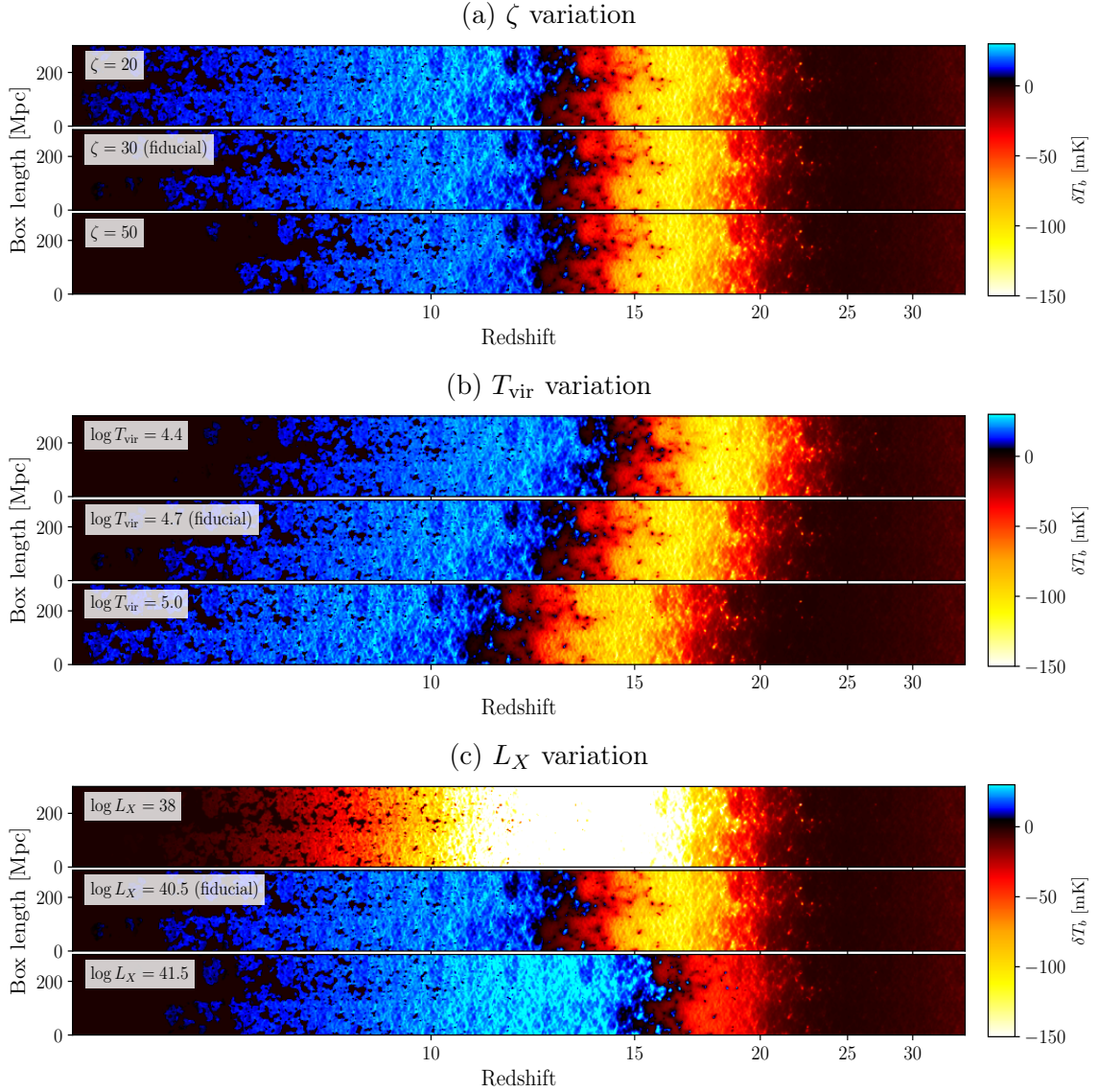


Figure 10: The simulated lightcones of the brightness temperature of the 21 cm signal for variations in ζ , T_{vir} and L_X .

structure formation from being dominated by faint, low-mass galaxies to bright, massive galaxies through modifications to the HMF. Consequently, bump models may exhibit degeneracies with T_{vir} ; indeed, analysis using the global 21 cm signal revealed that k_{peak} produces degenerate effects with T_{vir} [22]. We examine whether morphological analysis can break this degeneracy below.

- **L_X :** Variations in L_X produce effects that are highly distinguishable from the fiducial model. Since X-ray luminosity heats the IGM, higher L_X rapidly elevates the kinetic temperature T_K above T_γ , which couples to T_S and results in earlier emission signals. These effects are particularly significant at $z \lesssim 20$.

5.2 Quantifying morphological differences

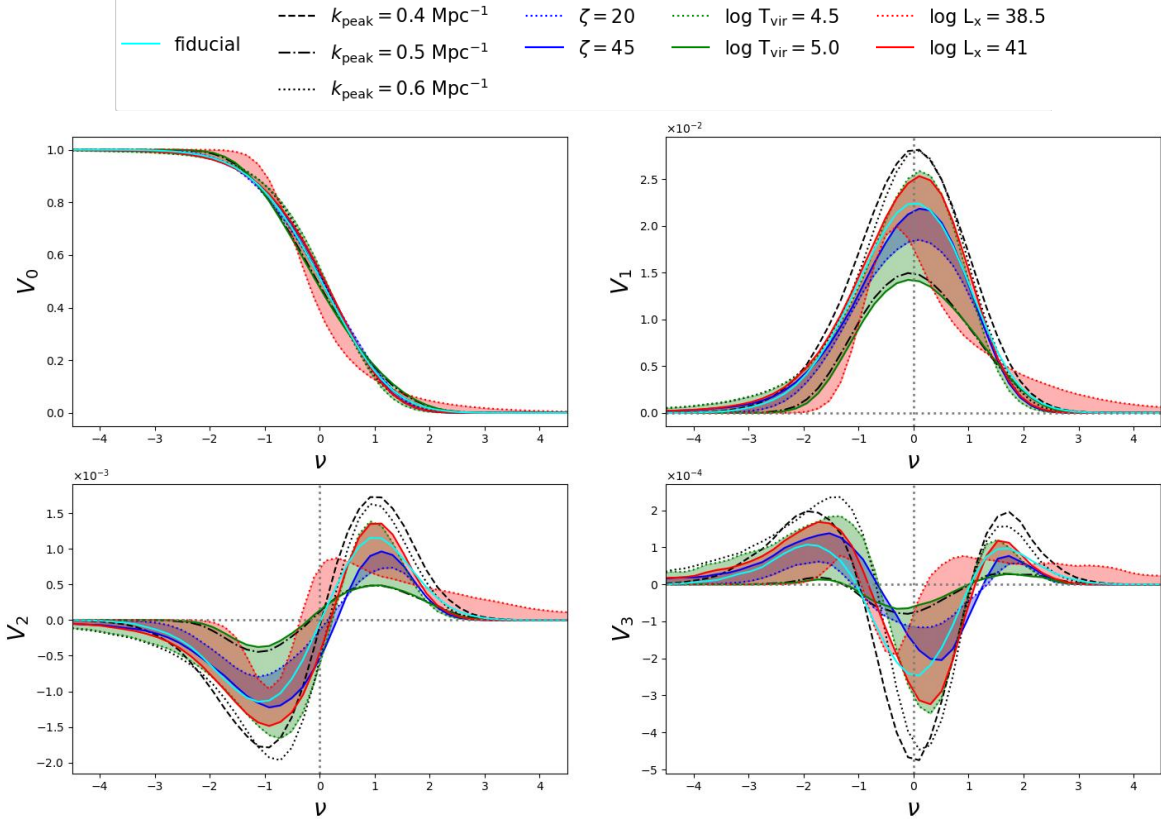


Figure 11: The MFs of the brightness temperature field for all models considered in this work, shown at $z = 11$. The solid cyan line represents the fiducial model, while dashed, dash-dotted, and dotted lines correspond to bump models with $k_{\text{peak}} = 0.4, 0.5$, and 0.6 Mpc^{-1} , respectively. The shaded regions in blue, green, and red enclose the MFs spanning the full parameter ranges of ζ , T_{vir} , and L_X listed in table 1.

We now jointly study the signatures of bump models and EoR scenarios to discern their distinct signatures, focusing only on the observable brightness temperature field. We vary the bump model parameter k_{peak} and EoR parameters as specified in table 1. The bump amplitude is fixed to be $A_I = 10^{-8}$. All results shown in this section are for this value. In figure 11, we plot the MFs of the brightness temperature field for all models: fiducial, bump models, and EoR scenarios (with shaded regions spanning the range between minimum and maximum values of EoR parameters in table 1) at redshift $z = 11$. We chose this redshift for visual representation simply because it roughly corresponds to the midpoint of reionization for most models and thus includes contributions from all constituent fields in eq. (2.4). As can be seen visually, the shapes of V_1 , V_2 , and V_3 vary significantly across models, with visible differences in peak heights and curve asymmetry.

For V_1 , the maximum near $\nu = 0$ has the highest amplitude for the $k_{\text{peak}} = 0.6 \text{ Mpc}^{-1}$ model, followed by other models in decreasing order, with the fiducial model exhibiting the lowest amplitude. The V_1 curves are not symmetric about $\nu = 0$; for example, the $\log L_X = 38.5$ curve is skewed toward negative thresholds, while the $\zeta = 45$ curve is skewed toward

positive thresholds. This asymmetry can be quantified by comparing the areas under the curve on the positive and negative threshold sides. For V_2 , the relative amplitudes of maxima and minima differ across models. The $k_{\text{peak}} = 0.6 \text{ Mpc}^{-1}$ curve exhibits the largest difference between its maximum and minimum, while the fiducial curve shows the smallest. Additionally, the V_2 curves are asymmetric about the x -axis line (horizontal black dotted line). For V_3 , shown in the bottom right panel of figure 11, the maxima at positive and negative threshold values have different amplitudes. For instance, in the $k_{\text{peak}} = 0.6 \text{ Mpc}^{-1}$ model, the maximum at negative thresholds has a higher amplitude than that at positive thresholds, whereas this behaviour is reversed for the $k_{\text{peak}} = 0.4 \text{ Mpc}^{-1}$ model. The V_3 curves are asymmetric about the y -axis line (vertical black dotted line).

These observations motivate the definition of derived measurable quantities by condensing the amplitude and shape information of V_1 , V_2 , and V_3 , so as to extract the distinct signatures of different models. The amplitude quantifiers \mathcal{A}_i are defined as:

$$\mathcal{A}_1 = V_1^{\max}, \quad (5.1)$$

$$\mathcal{A}_2 = V_2^{\max} + |V_2^{\min}|, \quad (5.2)$$

$$\mathcal{A}_3 = \frac{V_3^{\max,+} - V_3^{\max,-}}{V_3^{\max,+} + V_3^{\max,-}}, \quad (5.3)$$

where V_1^{\max} is the maximum of each V_1 curve, $V_2^{\max/\min}$ are the maximum and minimum respectively of each V_2 curve, and $V_3^{\max,+}$ ($V_3^{\max,-}$) is the maxima of each V_3 curve located at positive (negative) threshold.

To capture the shape information, we use integrals of the MF curves in suitable threshold ranges. To define the integration limits we introduce the following special thresholds: $\nu_{\min/\max} = \mp 5$ which are the minimum and maximum thresholds considered here, ν_c is the threshold where the V_2 curves cross zero (each curve crosses zero only once in the vicinity of $\nu = 0$), and ν_- (ν_+) is the threshold value where the V_3 curves cross zero from positive to negative (negative to positive) values (V_3 curves cross zero at two points). These special thresholds vary from model to model. Then we define the shape quantifiers \mathcal{E}_i as:

$$\mathcal{E}_1 = \int_0^{\nu_{\max}} V_1(\nu) d\nu - \int_{\nu_{\min}}^0 V_1(\nu) d\nu, \quad (5.4)$$

$$\mathcal{E}_2 = \int_{\nu_c}^{\nu_{\max}} V_2(\nu) d\nu - \int_{\nu_{\min}}^{\nu_c} V_2(\nu) d\nu, \quad (5.5)$$

$$\mathcal{E}_3 = \frac{\left(\int_{\nu_+}^{\nu_{\max}} V_3(\nu) d\nu - \int_{\nu_{\min}}^{\nu_-} V_3(\nu) d\nu \right)}{\left(\int_{\nu_+}^{\nu_{\max}} V_3(\nu) d\nu + \int_{\nu_{\min}}^{\nu_-} V_3(\nu) d\nu \right)}. \quad (5.6)$$

These six parameters \mathcal{A}_i , \mathcal{E}_i probe different aspects of the field morphology: \mathcal{A}_i measure information about amplitudes of the MFs and which are related to structural scales, while \mathcal{E}_i measures information associated with asymmetries and shapes of the MFs. Note that we do not include information from V_0 since it is known to have large cross-correlations across different thresholds relative to other MFs, rendering it difficult to construct its likelihood function and covariance matrix (see ref. [63] for details).

For the estimation of statistical uncertainties, we generate 30 simulations with different random seeds for each model. MFs are calculated from all the simulations, and then the means

and standard deviations of all the derived quantities defined in eqs. 5.1 to 5.6 are computed. This is plotted in the upper panels of figure 12 and 13. To quantify the distinguishability of the different models, for each derived statistic at each redshift, we calculate the distance of the mean value for each model from the mean of the fiducial model in units of the standard deviation of the field. These distances are shown in the lower panels of figure 12 and 13. The shaded yellow bands mark the 5σ deviations from the fiducial model. We use this as a benchmark when we describe distinguishability of different models below.

We now discuss the salient features of figures 12 and 13 in three redshift ranges - high, intermediate and low. The ranges are chosen based on the dominant contributions to $\langle \delta T_b \rangle$ from different terms in eq. (2.4), as explained in section 2.2 (see figure 2).

High redshifts ($z > 20$): At these high redshifts, the 21 cm signal is dominated by density field, as ionising sources are sparse. Consequently, most bump models are distinguishable from both fiducial and EoR models. Among the amplitude quantifiers, \mathcal{A}_1 and \mathcal{A}_2 exhibit similar behaviour: the $k_{\text{peak}} = 0.4 \text{ Mpc}^{-1}$ model becomes distinguishable at higher than 5σ significance beyond $z = 20$, the $k_{\text{peak}} = 0.5 \text{ Mpc}^{-1}$ model beyond $z = 22$, and the $k_{\text{peak}} = 0.6 \text{ Mpc}^{-1}$ model beyond $z = 27$. For \mathcal{A}_3 , the $k_{\text{peak}} = 0.4 \text{ Mpc}^{-1}$ model is distinguishable in the range $21 < z < 26$, while $k_{\text{peak}} = 0.6 \text{ Mpc}^{-1}$ is distinguishable for $23 < z < 28$. Among the shape quantifiers, \mathcal{E}_2 shows that both the $k_{\text{peak}} = 0.5$ and 0.6 Mpc^{-1} models become distinguishable beyond $z = 27$. For \mathcal{E}_3 , the $k_{\text{peak}} = 0.4 \text{ Mpc}^{-1}$ model is distinguishable in the range $22 < z < 28$, and $k_{\text{peak}} = 0.6 \text{ Mpc}^{-1}$ beyond $z = 23$. Of the EoR parameters, T_{vir} shows degeneracy with k_{peak} in this redshift range. This high-redshift cosmic dawn regime offers the cleanest separation between primordial and astrophysical signatures, making it very well suited for constraining bump model parameters.

Intermediate redshifts ($10 < z < 20$): This regime spans the active phase of reionization, where the 21 cm signal receives contributions from all constituent fields. The interplay between primordial features and astrophysical processes makes the distinguishability of bump models more nuanced and strongly redshift-dependent. For the amplitude quantifiers \mathcal{A}_1 and \mathcal{A}_2 , the turnover-scale model ($k_{\text{peak}} = 0.5 \text{ Mpc}^{-1}$) is distinguishable only within a narrow window around $z \sim 16$, while the $k_{\text{peak}} = 0.6 \text{ Mpc}^{-1}$ model shows distinguishability in two separate windows: $10 < z < 12$ and $18 < z < 20$. For \mathcal{A}_3 , the $k_{\text{peak}} = 0.4 \text{ Mpc}^{-1}$ model is distinguishable over a broader range $13 < z < 19$, whereas $k_{\text{peak}} = 0.6 \text{ Mpc}^{-1}$ is distinguishable for $16 < z < 20$. For the shape quantifiers, \mathcal{E}_1 shows that $k_{\text{peak}} = 0.4 \text{ Mpc}^{-1}$ is distinguishable for $13 < z < 17$ and $k_{\text{peak}} = 0.6 \text{ Mpc}^{-1}$ for $16 < z < 20$. In \mathcal{E}_2 , the $k_{\text{peak}} = 0.4 \text{ Mpc}^{-1}$ model shows the broadest window of distinguishability ($14 < z < 20$), whereas $k_{\text{peak}} = 0.5 \text{ Mpc}^{-1}$ is distinguishable only near $z \sim 17$ and $k_{\text{peak}} = 0.6 \text{ Mpc}^{-1}$ for $18 < z < 20$. For \mathcal{E}_3 , the $k_{\text{peak}} = 0.4 \text{ Mpc}^{-1}$ model exhibits two windows of distinguishability ($10 < z < 13$ and $14 < z < 17$), the turnover-scale model is distinguishable only at $z \sim 17$, and the $k_{\text{peak}} = 0.6 \text{ Mpc}^{-1}$ model for $17 < z < 20$.

Low redshifts ($z < 10$): In this redshift range, the 21 cm signal morphology is dominated by ionised regions surrounding luminous sources. Variations in both ζ and L_X significantly affect the signal, leading to substantial overlap between EoR and bump model signatures. Consequently, bump models are distinguishable from EoR scenarios only in limited cases. For the amplitude quantifiers \mathcal{A}_1 and \mathcal{A}_2 , only the $k_{\text{peak}} = 0.4 \text{ Mpc}^{-1}$ model remains distinguishable, and only below $z \simeq 8$. For \mathcal{A}_3 and the shape quantifier \mathcal{E}_2 , the $k_{\text{peak}} = 0.6 \text{ Mpc}^{-1}$ model shows marginal distinguishability around $z \sim 8$.

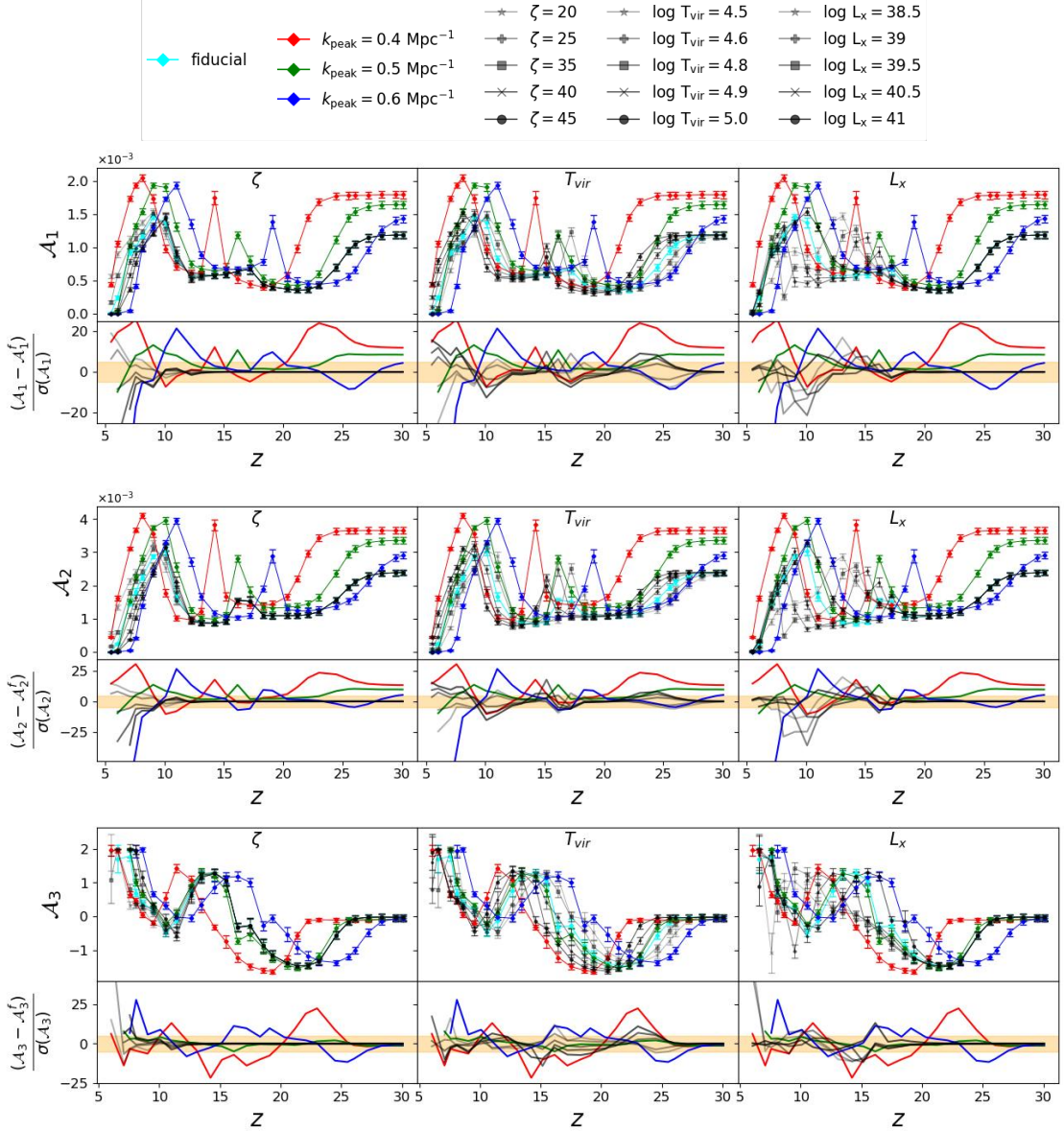


Figure 12: Redshift evolution of the amplitude parameters \mathcal{A}_1 , \mathcal{A}_2 , and \mathcal{A}_3 (defined in eqs. 5.1–5.3) for bump models and EoR parameter variations. The columns correspond to variations in ζ (left), T_{vir} (centre), and L_x (right). The upper panels in each row show the parameter values with 1σ error bars estimated from 30 realisations. The lower panels show the deviation of each model from the fiducial in units of the standard deviation. The colours and markers for bump models and EoR models are as indicated in the legend.

To summarize, bump models are robustly distinguished from EoR models at $z > 20$, where density fluctuations dominate and astrophysical processes have minimal impact. At intermediate redshifts ($10 < z < 20$), model sensitivities vary with the statistics used, with the turnover-scale model ($k_{\text{peak}} = 0.5 \text{ Mpc}^{-1}$) identifiable in specific redshift windows. At relatively low redshift ($z < 10$), we find degeneracy of bump and EoR parameters. However, there exists redshift windows where they can be distinguished for different statistics. Notably,

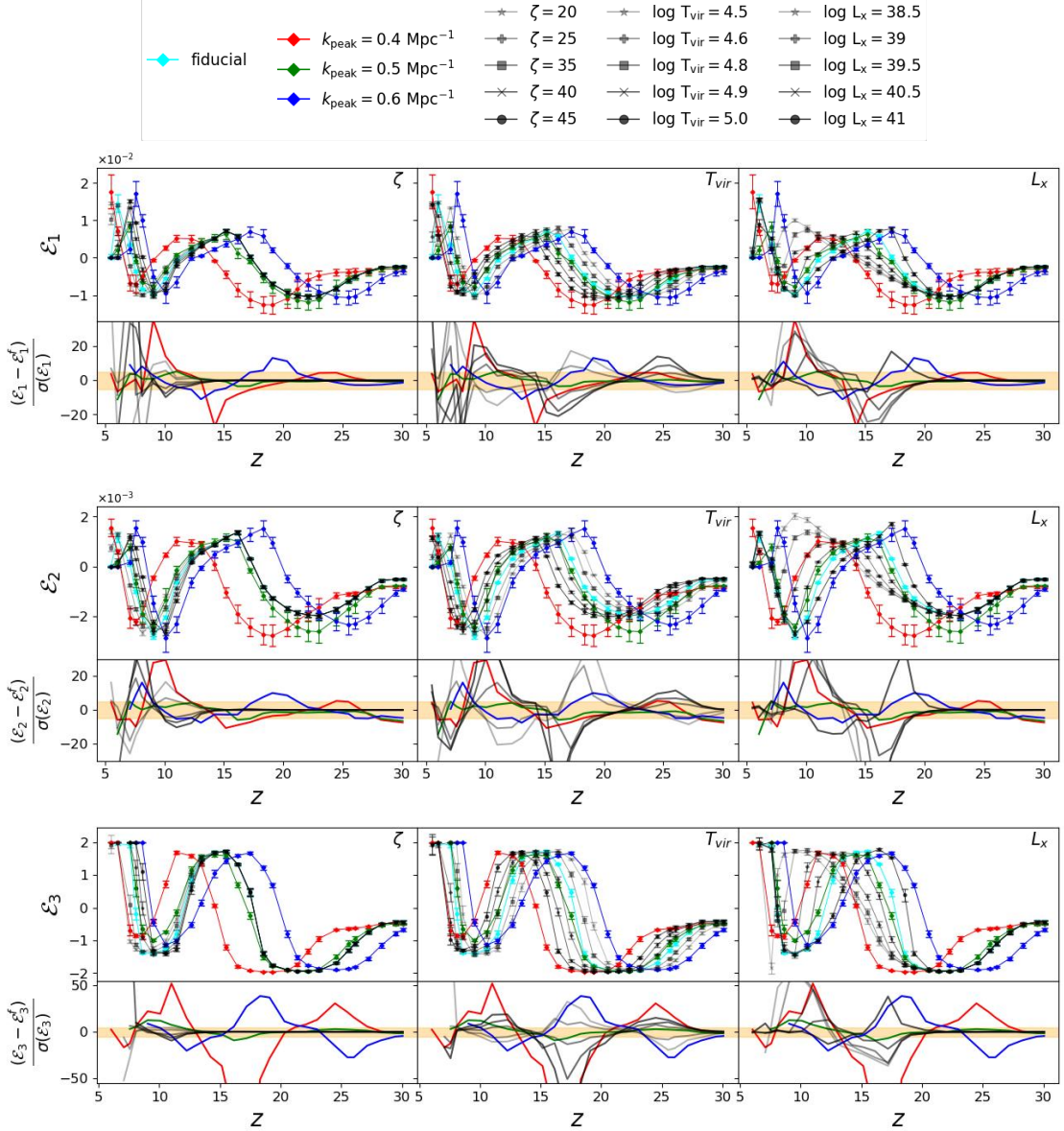


Figure 13: Same as figure 12, but for the shape parameters \mathcal{E}_1 , \mathcal{E}_2 , and \mathcal{E}_3 (defined in eqs. 5.4–5.6).

combining multiple statistics across redshifts can enhance the overall constraining power, as different k_{peak} values show complementary windows of distinguishability.

6 Summary and Discussion

In this work, we have explored the morphological signatures of bump-like primordial features arising from particle production during inflation on the 21 cm signal from cosmic dawn and the Epoch of Reionisation. The bump model is parameterised by the amplitude A_I and the scale corresponding to the peak of the feature, k_{peak} . We modified the initial power spectrum in the semi-numerical simulation code `21cmFAST` to incorporate bump-like features

and compared the resulting fields with a fiducial model that adopts the nearly scale-invariant power spectrum.

Our analysis proceeded in two parts. First, we demonstrated that Minkowski functionals of the 21 cm signal are sensitive to primordial bump-like features. We compared six bump models with three k_{peak} values – 0.4, 0.5, and 0.6 Mpc^{-1} and two A_I values – 10^{-9} and 10^{-8} with the fiducial case. We systematically examined how bump features modify the morphology of the constituent cosmological fields – density field δ_b , spin temperature T_S , and neutral hydrogen fraction x_{HI} – that collectively determine the morphology of the 21 cm brightness temperature δT_b . We found that bump-like features enhance overdensities at scales corresponding to k_{peak} , modifying the characteristic length scale of density structures and thereby increasing MF amplitudes. These modifications propagate through the halo mass function to affect the timing of structure formation, heating, and reionisation, leaving distinct imprints on the MFs of T_S , x_{HI} , and δT_b across different redshift regimes. Importantly, MFs can distinguish bump models at the turnover scale $k^{\text{turn}} = 0.5 \text{ Mpc}^{-1}$ from the fiducial model – a scale where the global 21 cm signal and reionisation history are indistinguishable [22].

In the second part, we investigated potential degeneracies between primordial signatures and astrophysical uncertainties by considering different EoR scenarios based on three key parameters: ζ , T_{vir} , and L_X . By defining measurable quantities derived from MFs that quantify amplitude ($\mathcal{A}_1, \mathcal{A}_2, \mathcal{A}_3$) and shape ($\mathcal{E}_1, \mathcal{E}_2, \mathcal{E}_3$) information (eqs. (5.1) – (5.6)), we identified redshift ranges where bump models can be distinguished from EoR models. We found that bump models are most robustly distinguished at $z > 20$ across all statistics, where density fluctuations dominate and astrophysical processes have minimal impact. At intermediate redshifts ($10 < z < 20$) and lower redshifts ($z < 10$) we found redshift windows, depending on the specific statistic and k_{peak} value, where the models can be distinguished. Such derived statistics can serve as statistics for model selection by comparing with observed data using a full Markov Chain Monte Carlo (MCMC).

Our results demonstrate that MFs carry characteristic signatures of primordial bump-like features that are distinct from both the fiducial model and EoR parameter variations. While the 21 cm power spectrum is also sensitive to bump-like features [21], MFs provide complementary information by probing the non-Gaussian morphological properties of the signal; a detailed analysis of bump model signatures in the 21 cm power spectrum will be presented in forthcoming work (Naik et al., in preparation). Importantly, 21 cm observations across multiple redshifts are essential for robustly identifying these signatures, as different redshift regimes provide complementary information. The upcoming SKA will map the 21 cm brightness temperature in three dimensions over the redshift range $6 < z < 30$, providing precisely the tomographic data required for morphological analysis.

This work represents a first step towards using MFs to probe primordial features in the 21 cm signal and extricate the physical implications. While we have accounted for sample variance by averaging over multiple realisations, our analysis uses idealised simulations without observational effects such as thermal noise and foreground contamination; incorporating these will be essential for assessing detectability with real data. Although we focused on bump-like features from particle production during inflation, this is the first study to explore the imprints of primordial features on the morphology of the 21 cm signal. The framework developed here is general and can be readily applied to other inflationary models predicting scale-dependent features. Such studies are important, as detection of primordial features would provide insights into the physics of the inflationary epoch beyond what is accessible from CMB observations alone.

In future works we plan to extend this analysis in several directions. We will incorporate realistic SKA mock data to assess the detectability of bump model signatures under observational conditions. We will also perform a full Bayesian inference analysis using MCMC methods to quantify the constraining power of MFs for the bump model parameters A_I and k_{peak} , jointly exploring the EoR parameter space to provide a more complete picture of potential degeneracies. Additionally, comparing with other statistics such as the power spectrum and bispectrum will further enhance the ability to disentangle primordial and astrophysical signatures. These developments will establish the full potential of morphological statistics for probing inflationary physics with upcoming 21 cm surveys.

Acknowledgements

The computational work in this paper was carried out using the NOVA cluster at the Indian Institute of Astrophysics, Bengaluru. The authors thank Kazuyuki Furuuchi for a careful reading of the manuscript and helpful comments. SSN acknowledges support from the SERB-NPDF (File No. PDF/2023/001469), Anusandhan National Research Foundation, Government of India.

A Effect of primordial bump-like features on the halo mass function

In section 4.1, we discussed how primordial bump-like features affect 21 cm signals through two mechanisms: (i) by modifying the density field via the matter power spectrum, and (ii) by influencing the neutral hydrogen and spin temperature fields through changes in the collapsed fraction of halos, which depends on the halo mass function (HMF). In this section, we provide a concise summary of the second mechanism. For a comprehensive analysis, we refer the reader to [22].

The halo mass function, $\frac{dn}{d \ln M} [\text{Mpc}^{-3}]$, quantifies the comoving number density of halos in the mass range M to $(M + dM)$, and can be written as [64]

$$\frac{dn}{d \ln M} = \frac{\rho_m}{M} \frac{-d(\ln \sigma)}{dM} \nu f(\nu), \quad (\text{A.1})$$

where ρ_m represents the average matter density at $z = 0$ and ν is the critical overdensity threshold. In 21cmFAST, the Sheth-Tormen formula [65] for the HMF is used to calculate the number density of halos via $\nu f(\nu)$. The variance of the initial density fluctuation field, $\sigma(M)$, is obtained by linearly extrapolating to the present epoch and smoothing with a filter $W(kR)$ of scale R , i.e.,

$$\sigma^2(R) = \frac{1}{2\pi^2} \int_0^\infty dk k^2 P_m(k) W^2(kR), \quad (\text{A.2})$$

where $P_m(k)$ is the matter power spectrum. In 21cmFAST, a real-space top-hat filter is used by default, whose Fourier transform is given by

$$W(kR) = 3 \left[\frac{\sin(kR) - (kR) \cos(kR)}{(kR)^3} \right], \quad (\text{A.3})$$

where the radius of the top-hat filter, R , and the enclosed mass M are related by

$$R(M) \equiv \left[\left(\frac{3}{4\pi} \right) \left(\frac{M}{\rho_m} \right) \right]^{1/3}. \quad (\text{A.4})$$

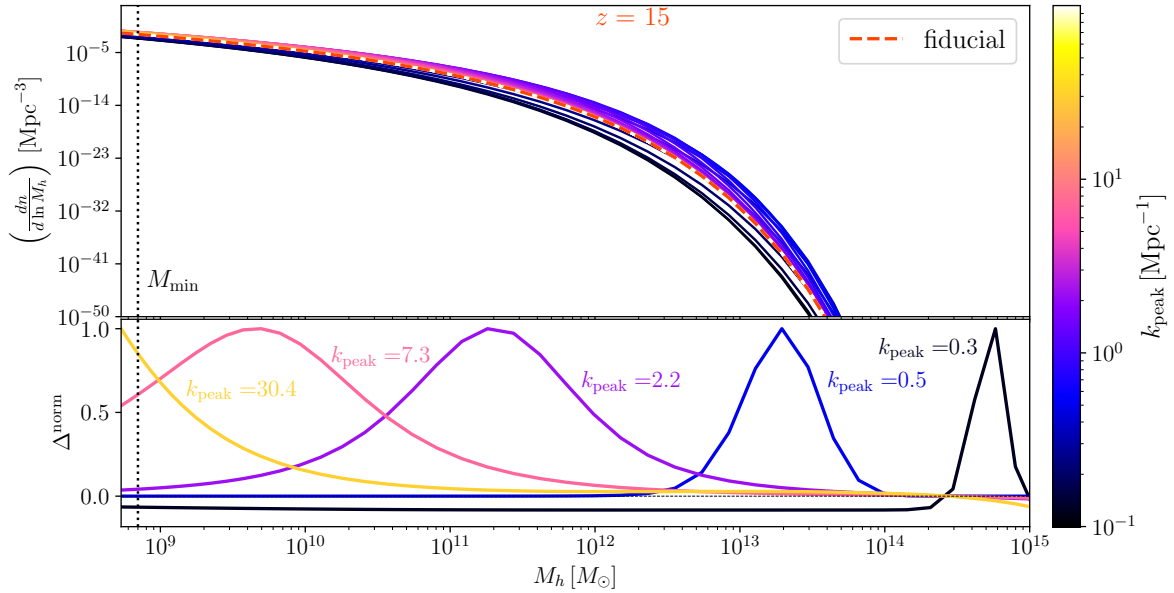


Figure 14: [Top] The halo mass function at $z = 15$, simulated using 21cmFAST for various bump models, with k_{peak} values shown in the color bar and the fiducial model indicated by the dashed line. [Bottom] The normalized relative difference of the HMF for the bump models with respect to the fiducial model, Δ^{norm} , for several values of k_{peak} . The vertical dashed line corresponds to the mass scale M_{min} .

From the above equations, it is evident that modifications to the power spectrum enter the halo mass function via the term $\sigma^2(M)$. The resulting halo mass functions for the bump models as simulated using 21cmFAST are plotted in figure 14. On the bottom panel, we also show Δ^{norm} – the relative difference between the bump and fiducial models, normalized by the maximum, for several values of k_{peak} . The plots indicate that bumps with lower values of k_{peak} increase the number density of high-mass halos and decrease the number density of low-mass halos. With increasing values of k_{peak} , the enhancement in the HMF shifts to lower mass scales. This anti-correlation between k_{peak} and M_{peak} (the mass corresponding to the peak in the HMF curve) arises from the fundamental relationship between wavenumbers and mass: a primordial bump-like feature with low k_{peak} affects large-scale fluctuations, and larger length scales correspond to larger mass scales (see eq. (A.4)).

The astrophysical implications of these HMF modifications become clear when considering the vertical dashed line in the figure, which corresponds to the mass scale M_{min} that sets the threshold above which halo collapse becomes important for reionization. Since low-mass halos in the vicinity of M_{min} dominate the collapse fraction and drive early structure formation, variations in their number density directly impact the timing of reionization. Consequently, a bump model with low k_{peak} (e.g., 0.3) decreases the number density of these critical low-mass halos, resulting in a lower collapsed fraction relative to the fiducial model and delayed structure formation and reionization. Conversely, a bump model with $k_{\text{peak}} = 7.3$ increases the number density of low-mass halos, producing a higher collapsed fraction and faster structure formation with earlier completion of reionization. Of particular interest is the “turnover scale” $k^{\text{turn}} = 0.5$, which predicts almost the same number density of low-mass halos as the fiducial model. Consequently, this model shows negligible changes in the collapsed

fraction and globally averaged quantities, as demonstrated in ref. [22]. The value of k^{turn} , however, uniquely depends on the choice of M_{\min} or T_{vir} .

References

- [1] S. Carniani, K. Hainline, F. D'Eugenio, D.J. Eisenstein, P. Jakobsen, J. Witstok et al., *Spectroscopic confirmation of two luminous galaxies at a redshift of 14*, *Natur* **633** (2024) 318 [[2405.18485](#)].
- [2] X. Fan, M.A. Strauss, R.H. Becker, R.L. White, J.E. Gunn, G.R. Knapp et al., *Constraining the evolution of the ionizing background and the epoch of reionization with $z \sim 6$ quasars. ii. a sample of 19 quasars*, *The Astronomical Journal* **132** (2006) 117.
- [3] S. Furlanetto, S.P. Oh and F. Briggs, *Cosmology at Low Frequencies: The 21 cm Transition and the High-Redshift Universe*, *Phys. Rept.* **433** (2006) 181 [[astro-ph/0608032](#)].
- [4] J.R. Pritchard and A. Loeb, *21-cm cosmology*, *Rept. Prog. Phys.* **75** (2012) 086901 [[1109.6012](#)].
- [5] J. Chluba, J. Hamann and S.P. Patil, *Features and New Physical Scales in Primordial Observables: Theory and Observation*, *Int. J. Mod. Phys. D* **24** (2015) 1530023 [[1505.01834](#)].
- [6] M.-L. Zhao, Y. Shao, S. Wang and X. Zhang, *Prospects for probing dark matter particles and primordial black holes with the Square Kilometre Array using the 21 cm power spectrum at cosmic dawn**, *Chin. Phys.* **50** (2026) 025101 [[2507.02651](#)].
- [7] H. Park, R. Barkana, N. Yoshida, S. Sikder, R. Mondal and A. Fialkov, *The signature of subgalactic dark matter clumping in the global 21-cm signal of hydrogen*, *Nature Astron.* **9** (2025) 1723 [[2509.11055](#)].
- [8] A. Cooray, C. Li and A. Melchiorri, *The trispectrum of 21-cm background anisotropies as a probe of primordial non-Gaussianity*, *Phys. Rev. D* **77** (2008) 103506 [[0801.3463](#)].
- [9] A. Pillepich, C. Porciani and S. Matarrese, *The bispectrum of redshifted 21-cm fluctuations from the dark ages*, *Astrophys. J.* **662** (2007) 1 [[astro-ph/0611126](#)].
- [10] J.B. Muñoz, Y. Ali-Haïmoud and M. Kamionkowski, *Primordial non-gaussianity from the bispectrum of 21-cm fluctuations in the dark ages*, *Phys. Rev. D* **92** (2015) 083508 [[1506.04152](#)].
- [11] P.D. Meerburg, M. Münchmeyer, J.B. Muñoz and X. Chen, *Prospects for Cosmological Collider Physics*, *JCAP* **03** (2017) 050 [[1610.06559](#)].
- [12] T. Flöss, T. de Wild, P.D. Meerburg and L.V.E. Koopmans, *The Dark Ages' 21-cm trispectrum*, *JCAP* **06** (2022) 020 [[2201.08843](#)].
- [13] D.J.H. Chung, E.W. Kolb, A. Riotto and I.I. Tkachev, *Probing Planckian physics: Resonant production of particles during inflation and features in the primordial power spectrum*, *Phys. Rev. D* **62** (2000) 043508 [[hep-ph/9910437](#)].
- [14] N. Barnaby, Z. Huang, L. Kofman and D. Pogosyan, *Cosmological Fluctuations from Infra-Red Cascading During Inflation*, *Phys. Rev. D* **80** (2009) 043501 [[0902.0615](#)].
- [15] N. Barnaby and Z. Huang, *Particle Production During Inflation: Observational Constraints and Signatures*, *Phys. Rev. D* **80** (2009) 126018 [[0909.0751](#)].
- [16] L. Pearce, M. Peloso and L. Sorbo, *Resonant particle production during inflation: a full analytical study*, *JCAP* **1705** (2017) 054 [[1702.07661](#)].
- [17] K. Furuuchi, *Excursions through KK modes*, *JCAP* **1607** (2016) 008 [[1512.04684](#)].
- [18] K. Furuuchi, S.S. Naik and N.J. Jobu, *Large Field Excursions from Dimensional (De)construction*, *JCAP* **06** (2020) 054 [[2001.06518](#)].

[19] K. Furuuchi, N.J. Jobu and S.S. Naik, *Extra-Natural Inflation (De)constructed*, [2004.13755](https://arxiv.org/abs/2004.13755).

[20] S.S. Naik, K. Furuuchi and P. Chingangbam, *Particle production during inflation: a Bayesian analysis with CMB data from Planck 2018*, *JCAP* **07** (2022) 016 [[2202.05862](https://arxiv.org/abs/2202.05862)].

[21] S.S. Naik, P. Chingangbam and K. Furuuchi, *Particle production during inflation: constraints expected from redshifted 21 cm observations from the epoch of reionization*, *JCAP* **04** (2023) 058 [[2212.14064](https://arxiv.org/abs/2212.14064)].

[22] S.S. Naik, P. Chingangbam, S. Singh, A. Mesinger and K. Furuuchi, *Global 21 cm signal: a promising probe of primordial features*, *JCAP* **05** (2025) 038 [[2501.02538](https://arxiv.org/abs/2501.02538)].

[23] H.W. Edler, F. de Gasperin and D. Rafferty, *Investigating ionospheric calibration for LOFAR 2.0 with simulated observations*, *A&A* **652** (2021) A37 [[2105.04636](https://arxiv.org/abs/2105.04636)].

[24] R.B. Wayth, S.J. Tingay, C.M. Trott, D. Emrich, M. Johnston-Hollitt, B. McKinley et al., *The Phase II Murchison Widefield Array: Design overview*, *PASA* **35** (2018) e033 [[1809.06466](https://arxiv.org/abs/1809.06466)].

[25] D.R. DeBoer et al., *Hydrogen Epoch of Reionization Array (HERA)*, *Publ. Astron. Soc. Pac.* **129** (2017) 045001 [[1606.07473](https://arxiv.org/abs/1606.07473)].

[26] <http://www.skatelescope.org/>.

[27] S. Bharadwaj and S.K. Pandey, *Probing non-Gaussian features in the HI distribution at the epoch of reionization*, *Mon. Not. Roy. Astron. Soc.* **358** (2005) 968 [[astro-ph/0410581](https://arxiv.org/abs/astro-ph/0410581)].

[28] H. Shimabukuro, S. Yoshiura, K. Takahashi, S. Yokoyama and K. Ichiki, *21 cm line bispectrum as a method to probe cosmic dawn and epoch of reionization*, *Mon. Not. Roy. Astron. Soc.* **458** (2016) 3003 [[1507.01335](https://arxiv.org/abs/1507.01335)].

[29] S. Majumdar, J.R. Pritchard, R. Mondal, C.A. Watkinson, S. Bharadwaj and G. Mellema, *Quantifying the non-Gaussianity in the EoR 21-cm signal through bispectrum*, *Mon. Not. Roy. Astron. Soc.* **476** (2018) 4007 [[1708.08458](https://arxiv.org/abs/1708.08458)].

[30] C.A. Watkinson, S.K. Giri, H.E. Ross, K.L. Dixon, I.T. Iliev, G. Mellema et al., *The 21-cm bispectrum as a probe of non-Gaussianities due to X-ray heating*, *Mon. Not. Roy. Astron. Soc.* **482** (2019) 2653 [[1808.02372](https://arxiv.org/abs/1808.02372)].

[31] A. Hutter, C.A. Watkinson, J. Seiler, P. Dayal, M. Sinha and D.J. Croton, *The 21 cm bispectrum during reionization: a tracer of the ionization topology*, *Mon. Not. Roy. Astron. Soc.* **492** (2020) 653 [[1907.04342](https://arxiv.org/abs/1907.04342)].

[32] L. Noble, M. Kamran, S. Majumdar, C.S. Murmu, R. Ghara, G. Mellema et al., *Impact of the Epoch of Reionization sources on the 21-cm bispectrum*, *JCAP* **10** (2024) 003 [[2406.03118](https://arxiv.org/abs/2406.03118)].

[33] H. Tomita, *Curvature Invariants of Random Interface Generated by Gaussian Fields*, *Progress of Theoretical Physics* **76** (1986) 952.

[34] K.R. Mecke, T. Buchert and H. Wagner, *Robust morphological measures for large-scale structure in the Universe*, *A&A* **288** (1994) 697 [[astro-ph/9312028](https://arxiv.org/abs/astro-ph/9312028)].

[35] J. Schmalzing and T. Buchert, *Beyond Genus Statistics: A Unifying Approach to the Morphology of Cosmic Structure*, *ApJ* **482** (1997) L1 [[astro-ph/9702130](https://arxiv.org/abs/astro-ph/9702130)].

[36] T. Matsubara, *Statistics of smoothed cosmic fields in perturbation theory. i. formulation and useful formulae in second-order perturbation theory*, *The Astrophysical Journal* **584** (2003) 1.

[37] L. Gleser, A. Nusser, B. Ciardi and V. Desjacques, *The morphology of cosmological reionization by means of minkowski functionals: Morphology of reionization*, *Monthly Notices of the Royal Astronomical Society* **370** (2006) 1329–1338.

[38] S. Yoshiura, H. Shimabukuro, K. Takahashi and T. Matsubara, *Studying topological structure of 21-cm line fluctuations with 3d minkowski functionals before reionization*, *Monthly Notices of the Royal Astronomical Society* **465** (2016) 394
[<https://academic.oup.com/mnras/article-pdf/465/1/394/8593179/stw2701.pdf>].

[39] K. Diao, Z. Chen, X. Chen and Y. Mao, *Reionization parameter inference from 3d minkowski functionals of the 21 cm signals*, *The Astrophysical Journal* **974** (2024) 141.

[40] S. Bag, R. Mondal, P. Sarkar, S. Bharadwaj and V. Sahni, *The shape and size distribution of H II regions near the percolation transition*, *MNRAS* **477** (2018) 1984 [[1801.01116](#)].

[41] S. Bag, R. Mondal, P. Sarkar, S. Bharadwaj, T.R. Choudhury and V. Sahni, *Studying the morphology of H I isodensity surfaces during reionization using Shapefinders and percolation analysis*, *MNRAS* **485** (2019) 2235 [[1809.05520](#)].

[42] R. Ghara, S. Bag, S. Zaroubi and S. Majumdar, *The morphology of the redshifted 21-cm signal from the Cosmic Dawn*, *Mon. Not. Roy. Astron. Soc.* **530** (2024) 191 [[2308.00548](#)].

[43] K.-G. Lee, R. Cen, J.R. Gott III and H. Trac, *The topology of cosmological reionization*, *The Astrophysical Journal* **675** (2008) 8.

[44] V. Ganesan and P. Chingangbam, *Tensor Minkowski Functionals: first application to the CMB*, *JCAP* **2017** (2017) 023 [[1608.07452](#)].

[45] P. Chingangbam, K.P. Yogendran, P.K. Joby, V. Ganesan, S. Appleby and C. Park, *Tensor Minkowski Functionals for random fields on the sphere*, *JCAP* **2017** (2017) 023 [[1707.04386](#)].

[46] S. Appleby, P. Chingangbam, C. Park, S.E. Hong, J. Kim and V. Ganesan, *Minkowski Tensors in Two Dimensions: Probing the Morphology and Isotropy of the Matter and Galaxy Density Fields*, *ApJ* **858** (2018) 87 [[1712.07466](#)].

[47] S. Appleby, P. Chingangbam, C. Park, K.P. Yogendran and P.K. Joby, *Minkowski Tensors in Three Dimensions: Probing the Anisotropy Generated by Redshift Space Distortion*, *ApJ* **863** (2018) 200 [[1805.08752](#)].

[48] A. Kapahtia, P. Chingangbam, S. Appleby and C. Park, *A novel probe of ionized bubble shape and size statistics of the epoch of reionization using the contour Minkowski Tensor*, *JCAP* **10** (2018) 011 [[1712.09195](#)].

[49] A. Kapahtia, P. Chingangbam and S. Appleby, *Morphology of 21cm brightness temperature during the epoch of reionization using contour minkowski tensor*, *Journal of Cosmology and Astroparticle Physics* **2019** (2019) 053.

[50] A. Kapahtia, P. Chingangbam, R. Ghara, S. Appleby and T.R. Choudhury, *Prospects of constraining reionization model parameters using Minkowski tensors and Betti numbers*, *JCAP* **05** (2021) 026 [[2101.03962](#)].

[51] C. Park, P. Pranav, P. Chingangbam, R. Van De Weygaert, B. Jones, G. Vegter et al., *BETTI Numbers of Gaussian Fields*, *Journal of Korean Astronomical Society* **46** (2013) 125 [[1307.2384](#)].

[52] S.K. Giri and G. Mellema, *Measuring the topology of reionization with betti numbers*, *Monthly Notices of the Royal Astronomical Society* **505** (2021) 1863–1877.

[53] W. Elbers and R. van de Weygaert, *Persistent topology of the reionization bubble network - I. Formalism and phenomenology*, *MNRAS* **486** (2019) 1523 [[1812.00462](#)].

[54] W. Elbers and R. van de Weygaert, *Persistent topology of the reionization bubble network - ii. evolution and classification*, *Monthly Notices of the Royal Astronomical Society* **520** (2023) 2709–2726.

[55] A. Mesinger, S. Furlanetto and R. Cen, *21CMFAST: a fast, seminumerical simulation of the high-redshift 21-cm signal*, *Mon. Not. Roy. Astron. Soc.* **411** (2011) 955 [[1003.3878](#)].

[56] S.G. Murray, B. Greig, A. Mesinger, J.B. Muñoz, Y. Qin, J. Park et al., *21cmFAST v3: A Python-integrated C code for generating 3D realizations of the cosmic 21cm signal*, *J. Open Source Softw.* **5** (2020) 2582 [[2010.15121](#)].

- [57] S.R. Furlanetto, S. Peng Oh and F.H. Briggs, *Cosmology at low frequencies: The 21cm transition and the high-redshift universe*, *Physics Reports* **433** (2006) 181–301.
- [58] G.B. Field, *Excitation of the Hydrogen 21-CM Line*, *Proceedings of the IRE* **46** (1958) 240.
- [59] S.A. Wouthuysen, *On the excitation mechanism of the 21-cm (radio-frequency) interstellar hydrogen emission line.*, *AJ* **57** (1952) 31.
- [60] C. Hikage, E. Komatsu and T. Matsubara, *Primordial non-gaussianity and analytical formula for minkowski functionals of the cosmic microwave background and large-scale structure*, *The Astrophysical Journal* **653** (2006) 11–26.
- [61] Z. Chen, Y. Xu, Y. Wang and X. Chen, *Stages of reionization as revealed by the minkowski functionals*, *The Astrophysical Journal* **885** (2019) 23.
- [62] A. Mesinger and S. Furlanetto, *Efficient Simulations of Early Structure Formation and Reionization*, *Astrophys. J.* **669** (2007) 663 [[0704.0946](#)].
- [63] M. Bashir, N. S. P. Chingangbam, F. Rahman, P. Goyal, S. Appleby et al., *Local patch analysis of ACT DR6 convergence map using morphological statistics*, *arXiv e-prints* (2025) [arXiv:2503.17849](#) [[2503.17849](#)].
- [64] W.H. Press and P. Schechter, *Formation of Galaxies and Clusters of Galaxies by Self-Similar Gravitational Condensation*, *ApJ* **187** (1974) 425.
- [65] R.K. Sheth and G. Tormen, *An Excursion Set Model of Hierarchical Clustering : Ellipsoidal Collapse and the Moving Barrier*, *Mon. Not. Roy. Astron. Soc.* **329** (2002) 61 [[astro-ph/0105113](#)].